CENTRO DE INVESTIGACIONES EN OPTICA, A.C.

University of Dayton

"GENERATION OF HYPERENTANGLED N00N STATES WITH RADIAL AND ORBITAL ANGULAR MOMENTUM LAGUERRE-GAUSS MODES AND DETECTION BASIS CONTROL"

Dual Program

Doctor of Sciences (Optics) from **Centro de Investigaciones en Óptica, A.C. (CIO)**

Doctor of Philosophy in Electro-Optics from **University of Dayton (UD)**

Final version

Includes changes suggested by the committee

Thesis presented by:

José César Guerra Vázquez

CIO Advisor: Dr. Roberto Ramírez Alarcón

UD Advisor: Dr. William N. Plick

Dec. 9, 2022

December 2022

León · Guanajuato · México

ABSTRACT

GENERATION OF HYPERENTANGLED N00N STATES WITH RADIAL AND ORBITAL ANGULAR MOMENTUM LAGUERRE-GAUSS MODES AND DETECTION-BASIS CONTROL

Name: Guerra Vazquez, Jose Cesar
University of Dayton

Advisor at CIO: Dr. Roberto Ramirez Alarcon
Advisor at UD: Dr. William N. Plick

Hyperentanglement of photonic light modes, or entanglement occurring in systems with one or more degrees of freedom, offers a valuable resource in quantum communication and information processing. Communication systems, for example, use hyperentanglement to increase channel capacity. Hyperentanglement, however, has not been the only valuable quantum resource. Maximally path-entangled states, or N00N states, have led the development of quantum information protocols. To advance quantum technology, it is necessary to establish reliable protocols that can generate both hyperentangled and N00N states. In this dissertation, we propose two methods for the generation of hyperentangled N00N states in the spatial degrees of freedom of light. The first approach centers on (but is not limited to) the radial degree of freedom of Laguerre-Gauss modes. In this study, the pump beam is shaped by superpositions of Laguerre-Gauss radial modes to generate hyperentangled radial N00N states via spontaneous parametric down-conversion. This method illustrates how the spatial spectrum of the down-converted state can be modulated by engineering the input pump. The resultant state, however, is noisy in nature and the cross-correlated terms limit the generation of clean, useful entangled states. The second method is a novel protocol based on the interference of two optical nonlinearities and the control of the detection basis in the orbital angular momentum degree of freedom. This configuration can

produce both maximally-entangled and hyper-entangled states in at least four dimensions. The resultant state in the four-dimensional case can be characterized as a generalization of the N00N state. As long as experimental imperfections are excluded, the production of this state is "perfect" i.e., noiseless. Using the presented setup, a vast parameter space of arbitrarily large dimensionality can be searched for other states of interest using control over the detection and pumping protocols. In addition, we demonstrate the versatility of this system through a few specific examples.

To my parents: Zenaida and Leonel.

To my siblings: Germán, Yesenia and Angela.

To Olivia.

TABLE OF CONTENTS

LIST OF FIGURES

CHAPTER I

INTRODUCTION

1.1 Historical context and motivation

Light is central to our daily lives and to the development of the most innovative technologies, such as lasers, LEDs, and solar power. Light has fascinated scientists for thousands of years, but the most significant breakthroughs in understanding occurred within the last one-hundred and fifty. At the end of the nineteenth century, light was thought to consist of waves of electromagnetic fields which propagated according to Maxwell's equations. However, not all the natural phenomena could be characterized as wavelike. Scientists realized that electromagnetic radiation also exhibits particle-like behavior and is emitted or absorbed only in tiny packets of energy called photons. The photon is a quantum of energy in the electromagnetic field, the carrier of electromagnetic forces.

The study of photons was of central importance to scientists in the twentieth century. Photons were first introduced by Planck as energy-quanta to make sense of black-body radiation [1]. Einstein used the concept of energy-quanta to explain the photo-electric effect and the wave-particle duality of light [2]. Compton built on these ideas to explain the now well-known Compton Scattering in which these light-quanta or photons behave like tiny billiard balls. Compton's work characterizes the scattering of photons after their interaction with stationary charged particles [3]. Thanks to the work of these minds and others, we know that all matter exhibits properties of both particles and waves, an idea first conceived by de Broglie [4]. The wave-particle nature of light and matter is fundamental to quantum physics and a pillar of our modern worldview.

In the last decades, photons have underpinned the development of photonic technologies now integral to daily life. Examples include advances in information technology such as free-space optical communications, fiber-optics networking, optical computing, and optical data processing and storage [5]. All of these innovations exploit the extremely long decoherence times of photons propagating at the speed of light. The minimal interaction of propagating photons with their environment makes them perfect candidates not only for exploring entanglement preservation, but also for the encoding of *qubits* in optical communication channels.

Procedures for quantum information processing and communication with entangled photons blossomed in the last decades. These advances are based on both exploitation of the photon's degrees of freedom to encode the information and the technological platforms able to generate, manipulate and detect single photons [6–9]. Quantum information can be encoded on a photon, for example, within polarization, optical path, time-bin, and orbital angular momentum degrees of freedom. Figure 1.1, taken from Ref. [10], illustrates how a photon can encode information based on these degrees of freedom. In the orbital angular momentum degree of freedom, for example, the most common tool used to encode the information is a spatial-light modulator (SLM). Figure 1.2 (from Ref. [10]) provides an example of some of the technological platforms, such as hardware, algorithms, and networks used in quantum communications. The blue dots illustrate a large-scale quantum network comprised of blind quantum computing, quantum repeaters for long-distance transmission, and quantum key distribution (QKD) managed by fiber networks or by free-space links.

Entangled photons have contributed to the development of quantum communication protocols. Among these protocols are quantum key distribution (QKD), superdense coding, quantum teleportation, and entanglement swapping. These key protocols enable the

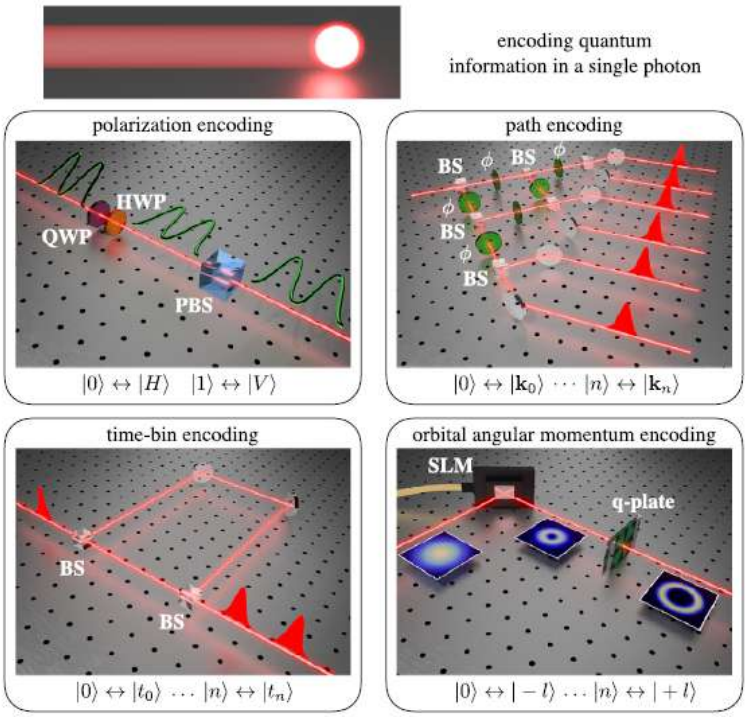

Figure 1.1: Encoding quantum information in a single photon exploiting different degrees of freedom. Possible choices include polarization (only a qubit of information can be carried in this case), path, time-bin and orbital angular momentum (larger dimensionalities can be reached). Legend—QWP: quarter-wave plate, HWP: half-wave plate, PBS: polarizing beam splitter, BS: beam splitter, ϕ: phase shift, SLM: spatial light modulator. Taken from Ref. [10], with copyright permission from the journal.

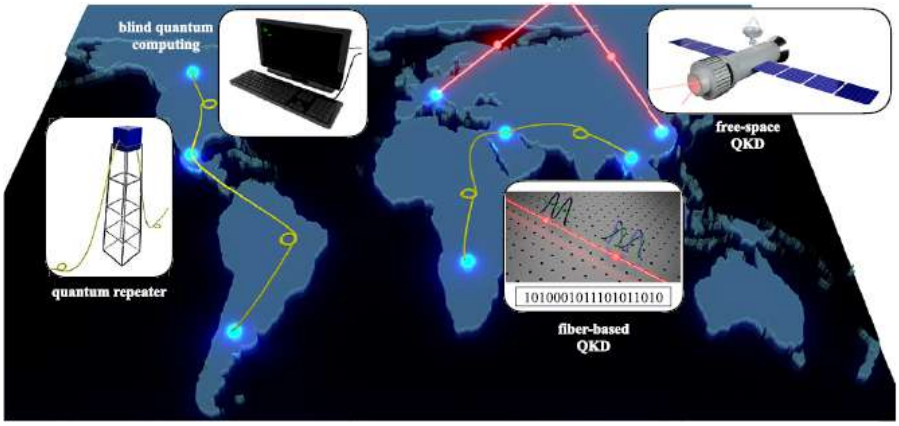

Figure 1.2: Schematic view of the main nodes in a large-scale quantum network, comprising blind quantum computing stages for the end user, quantum repeaters for long-distance transmission and quantum key distribution performed either via fiber networks or via free-space links. Taken from Ref. [10], with copyright permission from the journal.

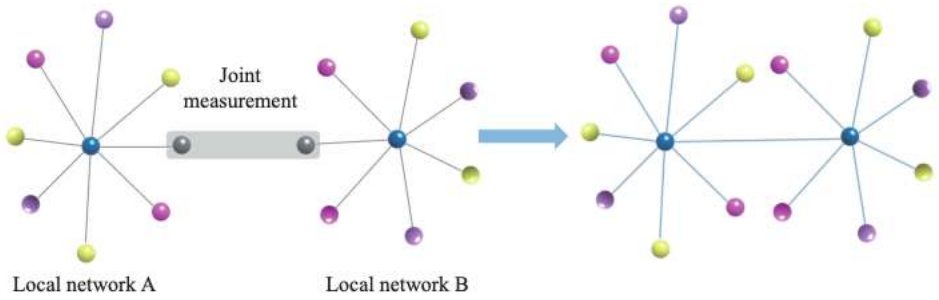

Figure 1.3: Entanglement swapping of two independent quantum networks. Taken from Ref. [11], with copyright permission from the journal.

deployment of next-generation global networks. Quantum networks offer substantial advantages over classical networks. In terms of security, QKD, for example, can utilize a classical communication channel and transform it into a secure channel by sending photons across an optical link. Observation of a quantum state causes perturbation in the communication, and any eavesdropper trying to observe the transmitted photons will disrupt the system causing transmission errors detectable to legitimate users [11–13].

Entanglement swapping is an important method in the construction of global quantum networks. Using this method, two independent entangled states are entangled without interacting directly. Entanglement swapping and quantum teleportation play an important role in the connection of nodes across the quantum network. Figure 1.3 shows an example of entanglement swapping demonstrated by Su et al. [11]. When entanglement swapping is performed, the two independent multipartite entangled states are merged into a larger entangled state which contains all unmeasured quantum modes.

A special interest in quantum computing revolves around the use of qubits to perform tasks difficult for classical computers. A qubit, or quantum bit, is the basic unit of information in quantum computing. The main difference between a bit and a qubit is that a

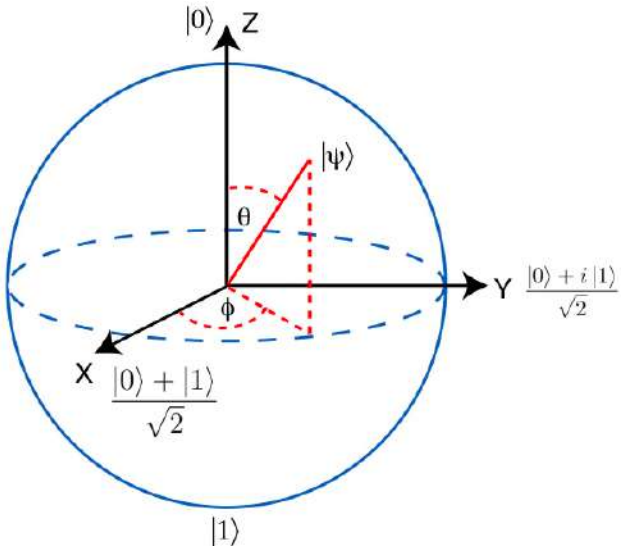

Figure 1.4: Geometrical representation of a qubit through a Bloch Sphere. Taken from https://www.quantum-inspire.com. The poles ($\theta = 0, \pi$) represent the states $|0\rangle$ and $|1\rangle$, respectively. Around the equator ($\phi = 0, 2\pi$; $\theta = \pi/2$) are the equally weighted superpositions of $|0\rangle$ and $|1\rangle$.

classical bit will only encode either 0 or 1, while a quantum bit can be both 0 and 1 at the same time. This phenomenon highlights the principles of superposition and entanglement inherent to quantum systems. Figure 1.4 shows a geometrical representation of a qubit. The North and the South poles ($\theta = 0, \pi$) represent the states $|0\rangle$ and $|1\rangle$, respectively. Around the equator ($\phi = 0, 2\pi$; $\theta = \pi/2$) are the equally weighted superpositions of $|0\rangle$ and $|1\rangle$. A quantum system can be in a superposition of all possible states at the same time, and these states can be entangled with each other. These quantum properties allow a system with N qubits to execute 2^N calculations in parallel. Quantum computers possess far greater capabilities than classical computers for processing, storing, and securing information [14, 15].

A natural extension of the two-dimensional quantum system, or qubit into a d-dimensional quantum system is the qudit. Exploration of high-dimensional quantum spaces has gained

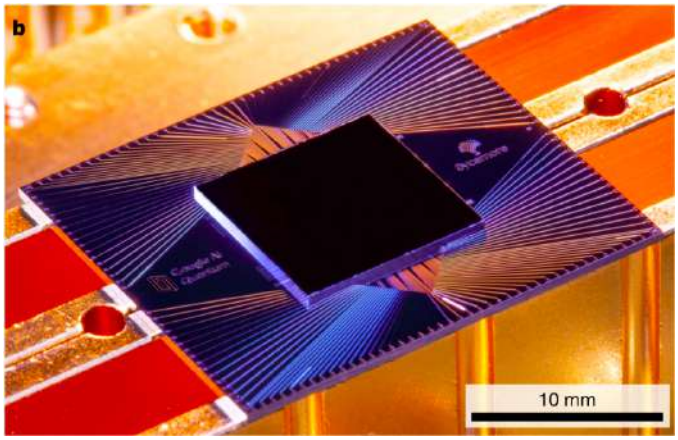

Figure 1.5: Photograph of the 53-qubits Sycamore Processor. Taken from Ref. [21], with copyright permission from the journal.

popularity over the last decade, a challenging research area that is rich in potential. The spatial modes of light, also known as structured light, offer a natural route toward high-dimensional quantum channels and spaces. Structured light provides a larger state-space to store and process information, as large as the experimental parameters tolerate [16–18]. In addition to increased noise tolerance and eavesdropping, qudits also allow higher information capacity per single photon: $log_2(d)$ *bits/photon*, where d is the dimensionality of the quantum space [19].

Quantum technology is also yielding incredible advances in computing. Entanglement allows computations to perform exponentially faster than any traditional computing method, a phenomenon known as quantum supremacy [20]. The Sycamore Processor (Figure 1.5) implemented by Arute et al. [21] provides an example of quantum supremacy with 53 qubits, representing a quantum state-space of 10^{16} dimensions. The powerful quantum processor takes about 200 seconds to sample one quantum circuit a million times, while a classical supercomputer would take approximately 10,000 years to complete this task!

Quantum computing is now a cutting-edge field, but it was conceived by Feynman over forty years ago. Feynman theorized that the only efficient simulation of a quantum system would come from another quantum system. He was first to suggest building a more powerful computer using quantum physics [22]. Following Feynman's ideas Grover demonstrated a faster algorithm for estimating the median from an N-element database search [23]. Shor built on these ideas to develop a quantum algorithm for prime factorization that is exponentially faster than all known classical algorithms [24].

Photonic systems are the most commonly used platforms for the development of quantum technologies. Great effort has been applied to the study and implementation of quantum protocols for these systems using entangled photons with dimensionalities beyond the two-dimensional limit of polarization. Focus areas include path, number, time, frequency, and the complex-spatial degrees of freedom of a photon, [16,25–27].

A large amount of research with spatial degrees of freedom has focused on the orbital angular momentum (OAM) of entangled photon pairs generated by spontaneous parametric down-conversion (SPDC) processes. The OAM of light is associated with the azimuthal phase of the complex electric field $e^{il\phi}$, and it carries a value of $l\hbar$ per photon, where l is the topological charge of the beam, [28–30].

In recent years, there have been theoretical and experimental demonstrations of maximally-entangled states (MESs) with OAM. The generation of high-dimensional maximally-entangled OAM states has been performed using a pump in a superposition of Laguerre-Gauss modes [31,32], and later, a broader and flatter OAM spectrum was produced by shaping the pump beam profile [33]. Applications of high-photon-number N00N states, or maximally path-entangled states, have also been investigated, including angular super-resolution, bunching

two photons into different OAM N00N states [34], and quantum information processing using entanglement in systems with multiple degrees of freedom, also known as hyperentangled states [35]. Furthermore, a source of hyperentangled states encoded in time-frequency and vector-vortex-structured modes was recently reported [36], as well as the measurement of a N00N state with 10^{12} spatio-temporal modes [37].

The preparation and measurement of high-dimensional maximally-entangled states with OAM is still challenging despite the aforementioned progress. Much of this difficulty can be attributed to the noisiness inherent in the down-conversion process for OAM. Every possible OAM mode is produced, so without post-selection or heralding, some unwanted terms in the density matrix are always non-zero.

In this dissertation, we propose two methods for the generation of hyperentangled N00N states in the spatial degrees of freedom of light. In the first method we generate hyperentangled radial N00N states by shaping the pump in superpositions of Laguerre-Gauss radial modes. This method illustrates how the spatial spectrum of the down-converted state can be modulated by engineering the input pump. The second method is a novel protocol for the generation of hyperentangled OAM N00N states with tunable dimensionality which in the four-dimensional case results in a perfect state. The intrinsic characteristic of this method is interference between two nonlinearities on two beam splitters with a general heralding (detection) protocol on two of the four resulting modes that we call *detection-basis control*.

1.2 Dissertation outline

The introduction provides a review of the literature on quantum information processing and communication where photonic quantum systems play an instrumental role. Our research is motivated by an overview of experimental demonstrations of quantum protocols in

low and high dimensions. We have a special interest in spatial degrees of freedom with radial and OAM modes. Chapter II outlines the theoretical background that is required for the generation of hyperentangled OAM N00N states. In Chapter III we present our method of the generation of hyperentangled N00N states with Laguerre-Gauss radial modes. Chapter IV introduces our protocol for hyperentanglement generation based on interference between two nonlinearities on two beam splitters. We also present a novel detection method that we call *detection-basis control*. In Chapter V we present several specific implementations of the *detection-basis control*, generating two, three, four, and even higher-dimensional hyperentangled OAM N00N states. The experimental implementation of our protocol is presented in Chapter VI. Chapter VII shows an outlook of our research and discuss future prospects. Finally, Chapter VIII provides a summary of our key findings and concluding remarks.

CHAPTER II

THEORETICAL FRAMEWORK

2.1 Transverse spatial modes of light

The description of electromagnetic phenomena is enclosed in Maxwell's equations, which in the case of free space that contain no free charges $\rho = 0$, and no free currents $\mathbf{J} = 0$, in SI units are given by

$$\nabla \cdot \mathbf{D} = 0 \tag{2.1}$$

$$\nabla \times \mathbf{E} + \frac{\partial \mathbf{B}}{\partial t} = 0 \tag{2.2}$$

$$\nabla \cdot \mathbf{B} = 0 \tag{2.3}$$

$$\nabla \times \mathbf{H} - \frac{\partial \mathbf{D}}{\partial t} = 0. \tag{2.4}$$

For an isotropic medium, the constitutive relations connecting the fields are simple linear relations

$$\mathbf{D} = \varepsilon \mathbf{E} \qquad \text{and} \qquad \mathbf{B} = \mu \mathbf{H}, \tag{2.5}$$

where $\mathbf{D}$ is the electric displacement, $\mathbf{H}$ is the magnetic field, $\mathbf{E}$ is the electric field, and $\mathbf{B}$ is the magnetic induction. The electric permittivity and the magnetic permeability of the medium are represented by ε and μ, respectively. We emphasize that $\mathbf{E}$ and $\mathbf{B}$ are the fundamental fields [38].

Maxwell's equations tell us that there exist traveling waves that represent the transport of energy from one point to another. To derive the mathematical representation of these traveling waves we assume solutions of Maxwell's equations with harmonic time dependence $e^{-i\omega t}$. Then combining equations (2.1)-(2.4) lead to the Helmholtz wave equation for the

electromagnetic field

$$\left(\nabla^2 + k^2\right)\mathbf{E} \;=\; 0, \tag{2.6}$$

where k is the wavenumber $k = nc/\omega$. The quantity n is called the index of refraction and is related to the phase velocity of the wave $v = c/n$. The simplest solutions of Eq. (2.6) are the most fundamental electromagnetic waves, the plane waves

$$\mathbf{E}(\mathbf{x}) \;=\; \xi(\mathbf{x})e^{-i\mathbf{k}\cdot\mathbf{x}}\,\hat{\mathbf{e}}, \tag{2.7}$$

where $\mathbf{k} = (k_x, k_y, k_z)$ is the wavevector. The magnitude of $\mathbf{k}$ is the wavenumber k. The vector $\hat{\mathbf{e}} = (\hat{e}_x, \hat{e}_y, \hat{e}_z)$ is the basis vector.

To construct a paraxial wave in which their wavefront normals must be paraxial rays, we have to modulate the complex envelope $\xi(\mathbf{x})$ of the plane wave (2.7), making it a slowly vary function of position. So that, assuming that the wave propagates along the optical axis z, the complex amplitude of the modulated wave is given explicitly by the paraxial wave

$$E(\mathbf{x}) \;=\; \xi(\mathbf{x})e^{-ikz}. \tag{2.8}$$

For the paraxial wave (2.8) to satisfy the Helmholtz equation (2.6), the slowly-varying envelope approximation provides that

$$\left|\frac{\partial^2\xi}{\partial z^2}\right| \;\ll\; k\left|\frac{\partial\xi}{\partial z}\right|, \tag{2.9}$$

which leads to the complex envelope $\xi(\mathbf{x})$ must satisfy the Paraxial Helmholtz Equation or Paraxial Wave Equation (PWE)

$$\nabla_T^2\xi - i2k\frac{\partial\xi}{\partial z} \;=\; 0, \tag{2.10}$$

where $\nabla_T^2 = \partial^2/\partial x^2 + \partial^2/\partial y^2$ is the transverse Laplacian operator in Cartesian coordinates. The equation displayed in (2.10) has some similarity to the Schrödinger equation of quantum

physics

$$\left(-\frac{\hbar^2}{2m}\nabla^2 + V(\mathbf{x},t)\right)\Psi(\mathbf{x},t) - i\hbar\frac{\partial\Psi(\mathbf{x},t)}{\partial t} = 0. \tag{2.11}$$

Here, the complex wave function $\Psi(\mathbf{x},t)$ describes the behavior of a single particle of mass m in a potential energy $V(\mathbf{x},t)$ that characterizes the environment of the particle. The PWE (2.10) as well as the Schrödinger equation (2.11) have an infinity number of solutions, in principle at least. For the Schrödinger equation these solutions depend on the form of the potential energy. Take for example a potential independent of time which leads to the time-independent Schrödinger equation

$$\left(-\frac{\hbar^2}{2m}\nabla^2 + V(\mathbf{x})\right)\Psi(\mathbf{x}) = \mathrm{E}\Psi(\mathbf{x}), \tag{2.12}$$

where E is the energy of the system. Note that equation (2.12) is similar to the Helmholtz wave equation (2.6). The solutions of the time-independent Schrödinger equation describe stationary states that correspond to standing waves, and provide the allowed values of the energy E of the system. In the PWE (2.10) the potential $V(\mathbf{x})$ is zero, and the solutions depend on a given coordinate system in an inertial frame of reference, and are constructed base on the physical symmetry of the system. The fundamental solution, in cylindrical coordinates, is the Gaussian beam given by

$$E_G(\mathbf{x}) = \frac{w_0}{w(z)}\exp\left[-ikz - \frac{r^2}{w^2(z)} - ik\frac{r^2}{2R(z)} + i\phi_g(z)\right], \tag{2.13}$$

with beam parameters

$$w(z) = w_0\sqrt{1+\left(\frac{z}{z_0}\right)^2}, \tag{2.14}$$

$$R(z) = z\left[1+\left(\frac{z_0}{z}\right)^2\right], \tag{2.15}$$

$$\phi_g(z) = \tan^{-1}\left(\frac{z}{z_0}\right), \tag{2.16}$$

$$z_0 = \frac{\pi w_0^2}{\lambda}, \tag{2.17}$$

where z_0 is the Rayleigh range, $\phi_g(z)$ is the Gouy phase, $R(z)$ is the radius of the spherical wavefront, $w(z)$ is the beam width or beam radius, w_0 correspond to the beam width at $z = 0$, and $r = \sqrt{x^2 + y^2}$ is the radial position.

As we mentioned, the different solutions of the PWE (2.10) depend on the symmetry of the coordinate system. Some of the beamlike solutions result in different kinds of beams that exhibit helical wavefronts, that is, optical beams carrying orbital angular momentum (OAM). Examples of solutions carrying OAM are Laguerre-Gauss modes [39], Ince-Gauss modes [40], and non-diffracting beams such as Bessel modes [41], Airy modes [42] and Mathieu modes [43]. In the next sections and chapters we present some of these solutions. In particular, we exploit Laguerre-Gauss (LG) modes carrying an OAM of $l\hbar$ per photon in our protocol for "Generation of four-dimensional hyperentangled NOON states and beyond with photonic orbital angular momentum and detection-basis control" [44], which is introduced in the following chapters. We devote a whole chapter, Chapter III, to study the LG radial modal number and its applications to quantum information protocols.

2.2 Orbital angular momentum and the classical-quantum correspondence

It is well-known that light fields have angular momentum. In other words, light fields could carry spin angular momentum (SAM) and/or orbital angular momentum (OAM). This behavior is illustrated in Figure 2.1. SAM is associated with the polarization of the complex electric field and carries a spin momentum of $\pm\hbar$ per photon. OAM is intrinsic in the azimuthal phase of the complex electric field carrying a value of $l\hbar$ per photon, being l the topological charge of the beam, and can take infinite values. If a particle absorbs a beam carrying spin angular momentum it rotates around its own axis, while a particle absorbing orbital angular momentum rotates about the optical axis. [45, 46].

Spin Angular Momentum (SAM) Orbital Angular Momentum (OAM)

Figure 2.1: Angular momentum of light. Light fields have spin angular momentum (SAM) and/or orbital angular momentum (OAM). SAM is associated with the polarization of the complex electric field, and OAM is intrinsic in the azimuthal phase of the complex electric field. A particle that absorbs spin angular momentum rotates around its own axis, while a particle absorbing orbital angular momentum rotates about the optical axis. Taken from [47].

In this dissertation we focus on the OAM degree of freedom. In this degree of freedom the PWE (2.10) has simple sets of solutions in the form of optical beams. One of the most widely use are the Laguerre-Gauss (LG) beams which in cylindrical coordinates at z = 0 have the form [48]

$$\mathrm{LG}_p^l(\rho,\phi) = \frac{1}{w_0}\sqrt{\frac{2p!}{\pi(p+|l|)!}}\left(\frac{\rho\sqrt{2}}{w_0}\right)^{|l|} L_p^{|l|}\left(\frac{2\rho^2}{w_0^2}\right)\exp\left(\frac{-\rho^2}{w_0^2}\right)\exp\left(il\phi\right), \tag{2.18}$$

where the parameters are described as follows. The beam waist radius at $z = 0$ is described by w_0. The index l corresponds to the OAM $l\hbar$ per photon in the beam and describes the helical structure around a wave-front singularity, p is the number of radial nodes in the intensity distribution or, in terms of the intensity cross-section, $p + 1$ describes the number of concentric rings of radial intensity maxima, and $L_p^{|l|}(\cdot)$ is the associated Laguerre polynomial. ϕ and ρ are the azimuthal and radial coordinates, respectively.

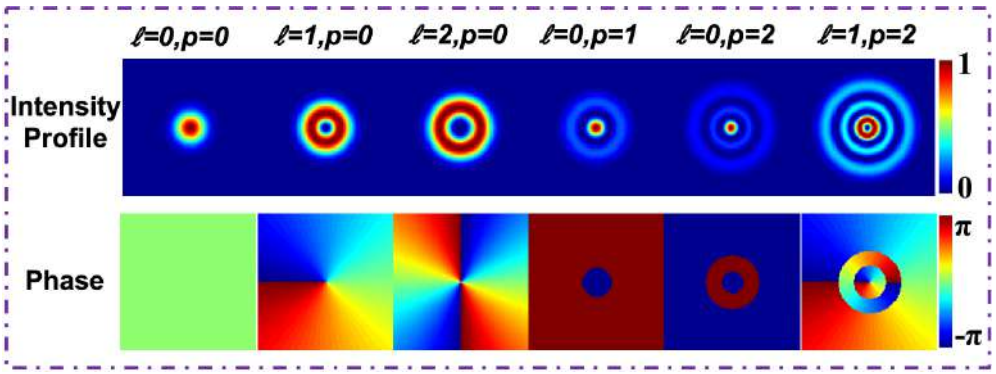

Figure 2.2: Transverse spatial profiles in both intensity and phase of several Laguerre-Gauss beams. Taken from Ref. [49].

Figure 2.2 shows the transverse spatial profiles in both intensity and phase of several Laguerre-Gauss beams, as found in Xie et al. [49]. As illustrated in the referenced figure, all beams with $l \neq 0$ have zero intensity at the beam center, and those with $p > 0$ take the form of multiple rings, while the phase rotation of the beam in the azimuthal direction is equal to $2\pi l$, and the radial structure displays p concentric discontinuities with no smooth transitions as opposed to the azimuthal direction.

Until now, we have presented optical beams carrying angular momentum from a classical point of view. To show the connection between classical and quantum beams carrying angular momentum we introduce the notion of *photon wave functions* through the Riemann-Silberstein vector formalism developed in [50].

Following Ref. [50] closely, we write the electromagnetic field in terms of the Riemann-Silberstein (RS) vector

$$\mathbf{F} = \sqrt{\frac{\varepsilon_0}{2}}(\mathbf{E} + ic\,\mathbf{B}), \tag{2.19}$$

where ε_0 is the permittivity of the vacuum, c is the speed of light in vacuum, and $\mathbf{E}$ and $\mathbf{B}$ are the electric and magnetic fields, respectively. In this formalism Maxwell's equations

reduce to two equations (see equations (2.1) - (2.4))

$$\nabla \cdot \mathbf{F}(\mathbf{x}, t) = 0, \tag{2.20}$$

$$\frac{\partial}{\partial t}\mathbf{F}(\mathbf{x}, t) = -ic\nabla \times \mathbf{F}(\mathbf{x}, t). \tag{2.21}$$

The electromagnetic field can be written using the gauge transformations

$$\mathbf{B}(\mathbf{x}, t) = \nabla \times \mathbf{A}(\mathbf{x}, t) \tag{2.22}$$

$$\mathbf{E}(\mathbf{x}, t) = -\frac{\partial \mathbf{A}(\mathbf{x}, t)}{\partial t} - \nabla\phi(\mathbf{x}, t) \tag{2.23}$$

where $\mathbf{A}(\mathbf{x}, t)$ and $\phi(\mathbf{x}, t)$ are the vector potential and scalar potential, respectively. Expressed in terms of the field potentials the Maxwell equations (2.1) - (2.4) become

$$\left(\frac{1}{c^2}\frac{\partial^2}{\partial t^2} - \nabla^2\right)\mathbf{A}(\mathbf{x}, t) = 0 \tag{2.24}$$

$$\left(\frac{1}{c^2}\frac{\partial^2}{\partial t^2} - \nabla^2\right)\phi(\mathbf{x}, t) = 0 \tag{2.25}$$

$$\nabla \cdot \mathbf{A}(\mathbf{x}, t) + \frac{1}{c^2}\frac{\partial \phi(\mathbf{x}, t)}{\partial t} = 0. \tag{2.26}$$

Substituting Eqs. (2.22) and (2.23) into Eq. (2.19), the RS vector takes the form

$$\mathbf{F}(\mathbf{x}, t) = \nabla \times \left(\frac{i}{c}\frac{\partial \mathbf{Z}(\mathbf{x}, t)}{\partial t} + \nabla \times \mathbf{Z}(\mathbf{x}, t)\right), \tag{2.27}$$

where $\mathbf{Z}(\mathbf{x}, t)$ is a generalized form of the two field potentials $\mathbf{A}(\mathbf{x}, t)$ and $\phi(\mathbf{x}, t)$. Expressed in terms of the field potentials the Maxwell equations (2.20) and (2.21) become

$$\left(\frac{1}{c^2}\frac{\partial^2}{\partial t^2} - \nabla^2\right)\mathbf{Z}(\mathbf{x}, t) = 0. \tag{2.28}$$

As we know, the simplest solutions of the wave equation are plane waves. To describe these solutions it is convenient to write $\mathbf{Z}$ in the form $\mathbf{Z}(\mathbf{x}, t) = (0, 0, 1)\chi(\mathbf{x}, t)$, where $\chi(\mathbf{x}, t)$ is, in general, a complex function that describes the true degrees of freedom of the electromagnetic

field. For the case of plane waves χ is a scalar function of the form

$$\chi(\mathbf{x},t) = \int d\mathbf{k} N(\mathbf{k}) \left(f^{+}(\mathbf{k}) e^{-i\omega_k t + i\mathbf{k}\cdot\mathbf{x}} + f^{-}(\mathbf{k}) e^{i\omega_k t - i\mathbf{k}\cdot\mathbf{x}} \right), \tag{2.29}$$

where $N(\mathbf{k})$ represents a normalization factor. Then the RS vector can be written as a superposition of plane waves given by

$$\mathbf{F}(\mathbf{x},t) = \int d\mathbf{k}\, \mathbf{e}(\mathbf{k}) \left(f^{+}(\mathbf{k}) e^{-i\omega_k t + i\mathbf{k}\cdot\mathbf{x}} + f^{-}(\mathbf{k}) e^{i\omega_k t - i\mathbf{k}\cdot\mathbf{x}} \right), \tag{2.30}$$

where $\mathbf{e}(\mathbf{k})$ is a normalized polarization vector that is determined by the choice of the vector part of the potential $\mathbf{Z}$. This exhibit the gauge freedom. $f^{\pm}(\mathbf{k})$ are two arbitrary complex amplitudes ($f^{-}(\mathbf{k}) = (f^{+}(\mathbf{k}))^{*}$), and $\omega_k = kc$ represents the oscillations of the electromagnetic field.

Our interest is in optical beams with angular momentum, so we have to rewrite the plane waves in Eq. (2.30) in a beamlike basis. We have to perform a change of basis from Cartesian coordinates to cylindrical coordinates, for instance. To do this we use the following expansion

$$e^{i\mathbf{k}\cdot\mathbf{x}} = e^{ik_z z} \sum_{m=-\infty}^{\infty} i^m\, e^{im(\phi - k_\phi)} J_m(k_\perp \rho), \tag{2.31}$$

where, in position space, ϕ and ρ are the polar and radial coordinates, respectively. k_ϕ is the polar coordinate in momentum space, and $k_\perp$ is both the transverse momentum and the radial coordinate in momentum space. The functions J_m are the Bessel functions of the first kind. In this case, plane waves become Bessel waves, and Eq. (2.29) transforms into

$$\begin{aligned}\chi(\mathbf{x},t) = \sum_{m=-\infty}^{\infty} \int_{-\infty}^{\infty} \frac{dk_z}{2\pi} \int_{0}^{\infty} \frac{dk_\perp}{2\pi} k_\perp \Big(& f^{+}_{mk_zk_\perp}\, \chi^{+}_{mk_zk_\perp}(\rho,\phi,z,t) \\ & + f^{-}_{mk_zk_\perp}\, \chi^{-}_{mk_zk_\perp}(\rho,\phi,z,t) \Big),\end{aligned} \tag{2.32}$$

where

$$\chi^{\pm}_{mk_zk_\perp}(\rho,\phi,z,t) = \frac{(\pm i)^m}{kk_\perp\sqrt{2}} e^{\mp i(\omega_k t - k_z z - m\phi)} J_m(k_\perp \rho), \tag{2.33}$$

and

$$f^{\pm}_{mk_zk_\perp} = \frac{1}{2\pi}\int_0^{2\pi} d\varphi\, f^{\pm}(\mathbf{k})e^{\mp im\varphi}. \tag{2.34}$$

Hence, the RS vector in the beamlike basis is given by

$$\mathbf{F}^{\pm}_{mk_zk_\perp}(\rho,\phi,z,t) = \frac{(\pm i)^m}{k\sqrt{2}}\, e^{\pm i(\omega_k t - k_z z - m\phi)} \begin{pmatrix} \pm ik_z \frac{\partial}{\partial(k_\perp\rho)} + i\frac{mk}{k_\perp\rho} \\ \mp k\frac{\partial}{\partial(k_\perp\rho)} - \frac{mk_z}{k_\perp\rho} \\ k_\perp \end{pmatrix} J_m(k_\perp\rho), \tag{2.35}$$

where k_z and $k_\perp$ ($-\infty < k_z < \infty$, $0 < k_\perp < \infty$) are the z and ρ components of the wave vector, respectively. The parameter m takes all integer values. These Bessel beams given by Eq. (2.35) are *exact solutions* of the Maxwell equations and form a complete set. Therefore, any other solution can be derived by combining Bessel beams linearly.

We have constructed beamlike functions using classical fields. The next step would be to construct photon wave functions through a similar procedure as described in the classical case, but using quantum fields as a means for connecting the classical and quantum functions respectively.

In quantum optics the RS vector takes the form of the field operator described by

$$\widehat{\mathbf{F}}(\mathbf{x},t) = \sqrt{\frac{\varepsilon_0}{2}}\left(\widehat{\mathbf{E}}(\mathbf{x},t) + ic\,\widehat{\mathbf{B}}(\mathbf{x},t)\right). \tag{2.36}$$

Following the model of harmonic oscillators in the canonical quantization of the electromagnetic field, we find the equal-time commutation relations

$$\begin{aligned} \left[\widehat{\mathbf{F}}_i(\mathbf{x},t), \widehat{\mathbf{F}}_j(\mathbf{x}',t)\right] &= 0, \\ \left[\widehat{\mathbf{F}}^{\dagger}_i(\mathbf{x},t), \widehat{\mathbf{F}}^{\dagger}_j(\mathbf{x}',t)\right] &= 0, \\ \left[\widehat{\mathbf{F}}_i(\mathbf{x},t), \widehat{\mathbf{F}}^{\dagger}_j(\mathbf{x}',t)\right] &= -\hbar c\epsilon_{ijk}\partial_k\delta^{(3)}(\mathbf{x}-\mathbf{x}'). \end{aligned} \tag{2.37}$$

To obtain plane waves we replace the classical field amplitudes in Eq. (2.30) by creation ($\hat{b}^\dagger$) and annihilation ($\hat{a}$) operators,

$$\widehat{\mathbf{F}}(\mathbf{x},t) = \sqrt{\hbar}\int d\mathbf{k}\,\mathbf{e}(\mathbf{k})\left(\hat{a}(\mathbf{k})e^{-i\omega_k t+i\mathbf{k}\cdot\mathbf{x}} + \hat{b}^\dagger(\mathbf{k})e^{i\omega_k t-i\mathbf{k}\cdot\mathbf{x}}\right), \tag{2.38}$$

where the operators $\hat{a}$ and $\hat{b}$ satisfy the following commutation relations

$$\begin{aligned}\left[\hat{a}(\mathbf{k}),\hat{a}^\dagger(\mathbf{k}')\right] &= (2\pi)^3\omega\delta^{(3)}(\mathbf{k}-\mathbf{k}'),\\ \left[\hat{b}(\mathbf{k}),\hat{b}^\dagger(\mathbf{k}')\right] &= (2\pi)^3\omega\delta^{(3)}(\mathbf{k}-\mathbf{k}').\end{aligned} \tag{2.39}$$

The operators $\hat{a}^\dagger(\mathbf{k})$ and $\hat{b}^\dagger(\mathbf{k})$ create different photons with opposite circular polarization.

Let's analyze the expansion of the RS field operator into beams carrying angular momentum. The steps are the same as in the classical case. The operator $\widehat{\mathbf{F}}(\mathbf{x},t)$ takes the form

$$\begin{aligned}\widehat{\mathbf{F}}(\mathbf{x},t) =& \sqrt{\hbar}\sum_{m=-\infty}^{\infty}\int_{-\infty}^{\infty}\frac{dk_z}{2\pi}\int_0^\infty\frac{dk_\perp}{2\pi}k_\perp\Big(\mathbf{F}^+_{mk_zk_\perp}(\rho,\phi,z,t)\,\hat{a}(m,k_z,k_\perp)\\ &+\mathbf{F}^-_{mk_zk_\perp}(\rho,\phi,z,t)\,\hat{b}^\dagger(m,k_z,k_\perp)\Big),\end{aligned} \tag{2.40}$$

where the new creation and annihilation operators $\hat{j}(m,k_z,k_\perp)$, with $j = a,a^\dagger,b,b^\dagger$, are defined as

$$\hat{j}(m,k_z,k_\perp) = \frac{1}{2\pi}\int_0^{2\pi}d\varphi\,e^{im\varphi}\,\hat{j}(\mathbf{k}). \tag{2.41}$$

The two functions $\mathbf{F}^{\pm}_{mk_zk_\perp}(\rho,\phi,z,t)$ are the *mode functions* of the electromagnetic field

$$\begin{aligned}\boldsymbol{\psi}^{+}_{mk_zk_\perp}(\rho,\phi,z,t) &= \mathbf{F}^{+}_{mk_zk_\perp}(\rho,\phi,z,t)\\ &= \frac{i^m}{k\sqrt{2}}\, e^{-i(\omega_k t - k_z z - m\phi)} \begin{pmatrix} ik_z \frac{\partial}{\partial(k_\perp\rho)} + i\frac{mk}{k_\perp\rho} \\ -k\frac{\partial}{\partial(k_\perp\rho)} - \frac{mk_z}{k_\perp\rho} \\ k_\perp \end{pmatrix} J_m(k_\perp\rho), \end{aligned} \tag{2.42}$$

$$\begin{aligned}\boldsymbol{\psi}^{-}_{mk_zk_\perp}(\rho,\phi,z,t) &= (\mathbf{F}^{-}_{mk_zk_\perp}(\rho,\phi,z,t))^*\\ &= \frac{i^m}{k\sqrt{2}}\, e^{-i(\omega_k t - k_z z - m\phi)} \begin{pmatrix} ik_z \frac{\partial}{\partial(k_\perp\rho)} - i\frac{mk}{k_\perp\rho} \\ k\frac{\partial}{\partial(k_\perp\rho)} - \frac{mk_z}{k_\perp\rho} \\ k_\perp \end{pmatrix} J_m(k_\perp\rho). \end{aligned} \tag{2.43}$$

Furthermore, $\mathbf{F}^{+}_{mk_zk_\perp}$ is the wave function $\boldsymbol{\psi}^{+}_{mk_zk_\perp}$ of the photon annihilated by $\hat{a}$, and $\mathbf{F}^{-}_{mk_zk_\perp}$ is the complex conjugate of the wave function $\boldsymbol{\psi}^{-}_{mk_zk_\perp}$ of the photon created by $\hat{b}^\dagger$. This leads to the more appropriate term of *photon wave functions*. Therefore, the wave functions $\boldsymbol{\psi}^{\pm}_{mk_zk_\perp}$ describe single-photon states and their *quantum numbers* may serve as *labels* characterizing the classical solutions. This exhibits the connection between the angular momentum of the classical beam and the angular momentum of a single photon characterized by the quantum numbers m in Eqs. (2.42) and (2.43).

2.3 Entangled states with the complex spatial modes of light via spontaneous parametric down-conversion

The most common method used to generate an entangled state in the photon's degrees of freedom is the spontaneous parametric down-conversion (SPDC) in a nonlinear crystal. In the SPDC process a photon from the pump interacting with the nonlinear crystal spontaneously splits in two daughter photons of lower energy called the signal photon and the idler photon. To achieve the maximal probability of the process all the photons must satisfy the

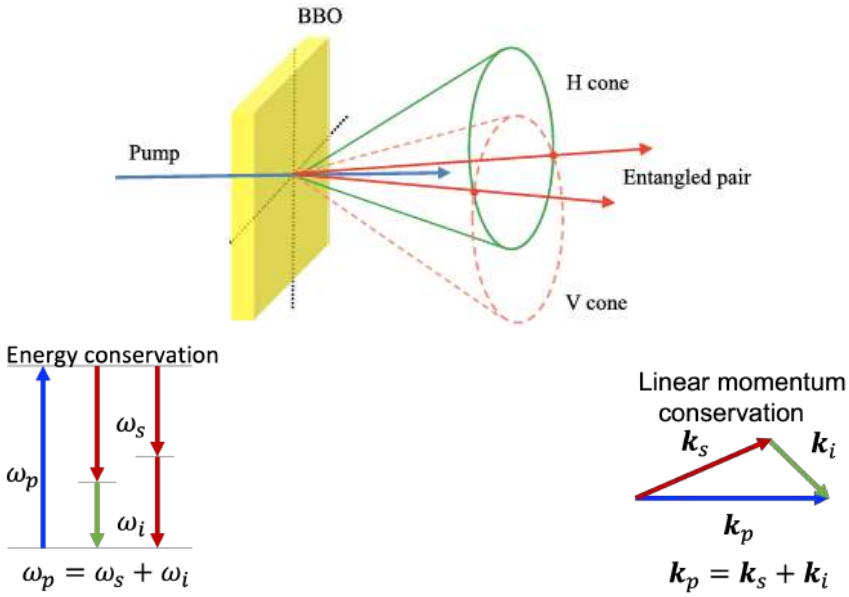

Figure 2.3: Spontaneous parametric down-conversion (SPDC) process in a nonlinear crystal (BBO), and phase matching conditions: energy and linear momentum conservation. $\mathbf{k}$ represents the wave vector and ω denotes the frequency. The subscripts p, s and i stand for the pump, signal, and idler photon, respectively. Taken from Ref. [35] with copyright permission from the journal.

phase matching conditions termed energy conservation and linear momentum conservation. Figure 2.3 illustrates the SPDC process and phase matching conditions. In the figure $\mathbf{k}$ represents the wave vector, and $\mathbf{k}_p = \mathbf{k}_s + \mathbf{k}_i$ denotes the linear momentum conservation. ω is the frequency of the photon, and the energy conservation is represented by the energy diagram and the equation $\omega_p = \omega_s + \omega_i$. The subscripts p, s and i stand for the pump, signal, and idler photon, respectively.

The fact that photons have well-defined OAM numbers, along with their negligible decoherence times, makes them ideal candidates for encoding large amounts of information. Even though the OAM space is an infinite-space, the finite amount of OAM information in an optical communication system is limited by the experimental space-bandwidth. However,

the usage of photons with OAM as information carriers results in a substantial advantage due to their natural large number of communication channels as compared to the capacity of any other traditionally used degrees of freedom such as polarization [51]. In addition to optical communications, light-beams carrying OAM have wide applications in quantum information processing, super-resolution imaging, optical tweezers, microscopy, metrology, biosensing and biomedicine. For further information we refer the interesting reader to check the review articles [10,47,52–55] which include many of the key papers.

In 2001, Zeilinger and coworkers [28] demonstrated that photon pairs generated in the SPDC process exhibit quantum entanglement and conservation of OAM. Their results conducted to a wide variety of experiments researching the generation, manipulation and measurement of single and entangled photons carrying OAM [6,16,18,26]. For example, to generate and analyze the desired OAM modes numerous devices have been developed, such as digital micro-mirror devices (DMD), spiral phase plates (SPP), and spatial-light modulators (SLM), that in combination with a single-mode fiber act as a mode filter allowing to measure the OAM of the photon with photo-detectors, or an ICCD camera triggered with a photo-detector [48].

Photon pairs generated by SPDC are entangled in the photon's degrees of freedom, such as polarization and the spatial degree of freedom. In the spatial degree of freedom the down-converted state can be describe as a superposition of Laguerre-Gauss (LG) modes (see Eq. (2.18)).

Following Ref. [44] closely, we write the down-converted entangled state, generated by a pump that is shaped in a single LG-mode $|l_{\rm p}, p_{\rm p}\rangle$, as

$$|\psi_{\rm SPDC}\rangle = \sum_{l_s,p_s}\sum_{l_i,p_i} B^{l_s,l_i}_{p_s,p_i}\,|l_s,\,p_s\rangle|l_i,\,p_i\rangle, \tag{2.44}$$

where the states $|l_s,\,p_s\rangle$ and $|l_i,\,p_i\rangle$ represent a photon pair in the signal and idler mode, respectively. The coefficients $|B^{l_s,l_i}_{p_s,p_i}|^2$ represent the probability to generate a photon pair with signal and idler modes given a pump with LG-mode $|l_{\rm p}, p_{\rm p}\rangle$, and the coincidence probability amplitudes of the same are given by the overlap integral [56]:

$$\begin{aligned} B^{l_s,l_i}_{p_s,p_i} &= \langle\psi_i,\psi_s|\,\psi_{\rm SPDC}\rangle \\ &= \int_0^{2\pi}\mathrm{d}\phi\int_0^{\infty}\rho\,\mathrm{d}\rho\,\mathrm{LG}^{l_{\rm p}}_{p_{\rm p}}(\rho,\phi)[\mathrm{LG}^{l_s}_{p_s}(\rho,\phi)]^*[\mathrm{LG}^{l_i}_{p_i}(\rho,\phi)]^*. \end{aligned} \tag{2.45}$$

If the entangled state is generated by a pump that is in a superposition of LG-modes then it is given by the superposition of the states generated by a pump with a single LG-mode, Eq. (2.44). So for that case we have

$$|\psi_{\rm pump}\rangle = \sum_{l_{\rm p},p_{\rm p}} a^{l_{\rm p}}_{p_{\rm p}}\,|l_{\rm p},p_{\rm p}\rangle. \tag{2.46}$$

The entangled state can be rewritten as

$$|\Psi_{\rm SPDC}\rangle = \sum_{l_s,p_s}\sum_{l_i,p_i} C^{l_s,l_i}_{p_s,p_i}\,|l_s,\,p_s\rangle|l_i,\,p_i\rangle, \tag{2.47}$$

where

$$C^{l_s,l_i}_{p_s,p_i} = \sum_{l_{\rm p},p_{\rm p}} a^{l_{\rm p}}_{p_{\rm p}}\,B^{l_{\rm p};\,l_s,l_i}_{p_{\rm p};\,p_s,p_i}. \tag{2.48}$$

These are the *full* coincidence amplitudes, where $B^{l_{\rm p};\,l_s,l_i}_{p_{\rm p};\,p_s,p_i}$ are the coincidence amplitudes given by Eq. (2.45), calculated for each *individual* Laguerre-Gauss component $|l_{\rm p}, p_{\rm p}\rangle$ of the initial pump.

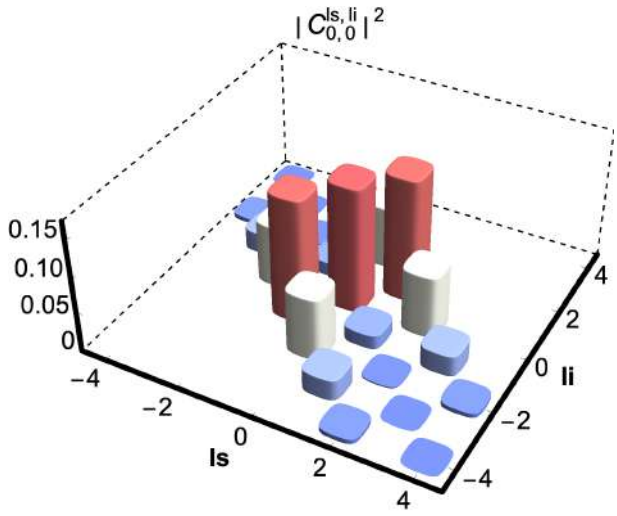

Figure 2.4: Spiral spectrum distributions of a three-dimensional maximally entangled state (MES). The x and y axes represent the azimuthal values of signal l_s photon and idler l_i photon, respectively, and the z axis represents the coincidence probability amplitudes $|C_{0,0}^{l_s,l_i}|^2$ of finding a photon pair with signal and idler modes $|l_s, l_i\rangle$. Those amplitudes on the diagonal (in red) constitute the target state, whereas other components are unwanted noise. Taken from Ref. [44], with copyright permission from the journal.

For example consider the case from Ref. [32], where the pump is put into a superposition of three pure azimuthal Laguerre-Gauss modes $|l_{\rm p}\rangle$, with complex amplitudes $a^{l_{\rm p}}$

$$|\psi_{\rm pump}\rangle = N\left(\sqrt{2.5}\,|-2\rangle + |0\rangle + \sqrt{2.5}\,|2\rangle\right), \tag{2.49}$$

where N is the normalization constant. The generated entangled state is a three-dimensional maximally entangled state (MES). The resulting probability amplitudes (density matrix) are shown in Figure 2.4. Note that the entangled state here is given by the diagonal elements (shown in red). The other amplitudes constitute unwanted noise.

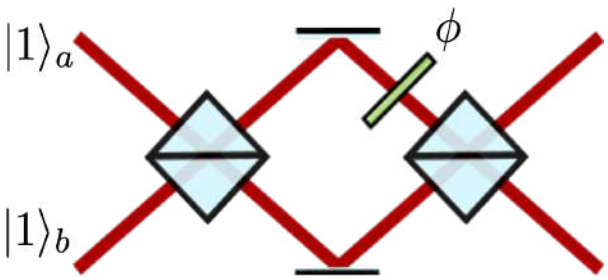

Figure 2.5: Diagram for enhancement in phase sensitivity. The states $|1\rangle_a$ and $|1\rangle_b$ are two input photons in modes a and b, respectively. The blue boxes represent 50:50 beam splitters. The element on green is a phase shift ϕ. The red lines illustrate the photon's paths. After interference on the second beam splitter we have an enhance in phase sensitivity that scales with the number of photons $\Delta\phi \sim 1/N$.

2.4 N00N states and hyperentangled states

N00N states are superpositions of path-entangled states of the form

$$|N00N\rangle = \frac{1}{\sqrt{2}}(|N\rangle_a|0\rangle_b + |0\rangle_a|N\rangle_b). \tag{2.50}$$

The first term has N photons in mode a with zero photons in mode b, while the second term has zero photons in mode a with N photons in mode b.

N00N states have been widely use in quantum information processing, metrology, and to enhance the phase sensitivity of interferometers [29, 57, 58]. To achieve an enhance in phase sensitivity, for example, we consider the diagram shown in Figure 2.5. The blue boxes represent two symmetric beam splitters. The states $|1\rangle_a$ and $|1\rangle_b$ are two input photons in modes a and b, respectively. The element on green represents a phase shift ϕ in one of the arms. The red lines illustrate the paths of the photons. So, for phase sensitivity enhancement, we bring two photons in modes a and b in the first beam splitter, being $|1\rangle_a|1\rangle_b$ the incident state. Thus, after beam splitter transformations we may write the

state

$$|N00N\rangle = \frac{1}{\sqrt{2}}(|2\rangle_a|0\rangle_b + |0\rangle_a|2\rangle_b), \tag{2.51}$$

which is a N00N state that has two photons in mode a with zero photons in mode b, and vice versa. Note that the two photons emerge together for either output-port of the beam splitter, and never leave the beam splitter separately through different output-ports. This is the so-called HOM effect, since Hong, Ou, and Mandel were first performing the experimental demonstration of this effect [59]. Sec. 4.1 discuss the HOM-effect in detail. Then, we put another beam splitter, and after interference we have an enhance in phase sensitivity that scales with the number of photons [60]

$$\Delta\phi \sim \frac{1}{N}. \tag{2.52}$$

The more photons we use, the better the phase sensitivity.

If in the aforementioned process we use two input photons entangled within their orbital angular momentum, after interference in the first beam splitter, we have an OAM N00N state

$$|N00N\rangle = \frac{1}{\sqrt{2}}(|l\rangle_a|0\rangle_b + |0\rangle_a|l\rangle_b), \tag{2.53}$$

where l is the OAM number. The first term of this OAM N00N state has two photons in mode a with OAM l and zero photons in mode b. Similarly, the second term has zero photons in mode a and two photons in mode b with OAM l. At the output of the second beam splitter in Figure 2.5 we get angular super-sensitivity [61]

$$\Delta\theta \sim \frac{1}{lN}, \tag{2.54}$$

which scales with the number of photons N and with the OAM quantum number l. The more OAM modes we use, the better the angular sensitivity for a fixed number of photons.

In this dissertation, we are interested in the generation of hyperentangled N00N states in the orbital angular momentum (OAM) degree of freedom via a SPDC process. Hyperentanglement occurring in systems with one degree of freedom is high-dimensional entanglement. If the quantum system has several degrees of freedom, hyperentanglement is the entanglement in the multiple degrees of freedom simultaneously. For example, a system can be hyperentangled in polarization, momentum, and time-energy, or combinations of them. Ref. [35] shows a review of this.

CHAPTER III

HYPERENTANGLED STATES WITH LAGUERRE-GAUSS RADIAL MODES

3.1 Down-conversion and Laguerre-Gauss radial modes

In this chapter we review the current state-of-the-art on the radial quantum number of Laguerre-Gauss modes, and present our approach for the generation of hyperentangled N00N states with radial modes.

The orbital angular momentum (OAM) of light has received a lot of attention in both classical and quantum regimes since Allen and co-workers [62] demonstrated that LG modes carry an OAM of $l\hbar$ per photon along the propagation direction. In the quantum domain, nonlinear interactions involving not only polarization and energy, but also several degrees of freedom such as the transverse profile of a single photon have become crucial in the implementation of novel quantum protocols and quantum communication systems in high-dimensional spaces. An example of this is the variety of quantum information protocols and their applications to quantum communication schemes based on the OAM of light [10, 16, 35, 63]. Radial modes of light, however, have not been investigated as OAM modes. Even though, in a similar way to OAM, high-dimensional quantum spaces can be explored through radial modes leading to potential applications in quantum information processing as we discuss below.

Although the study of the spatial structure of light initially focuses on the generation and detection of the azimuthal component of LG modes, over the last decade research on the forgotten radial quantum number [64] has been gradually gaining attention, showing several experimental demonstrations and theoretical investigations. To date, the radial mode entanglement has been characterized through full quantum state tomography in a 4-dimensional

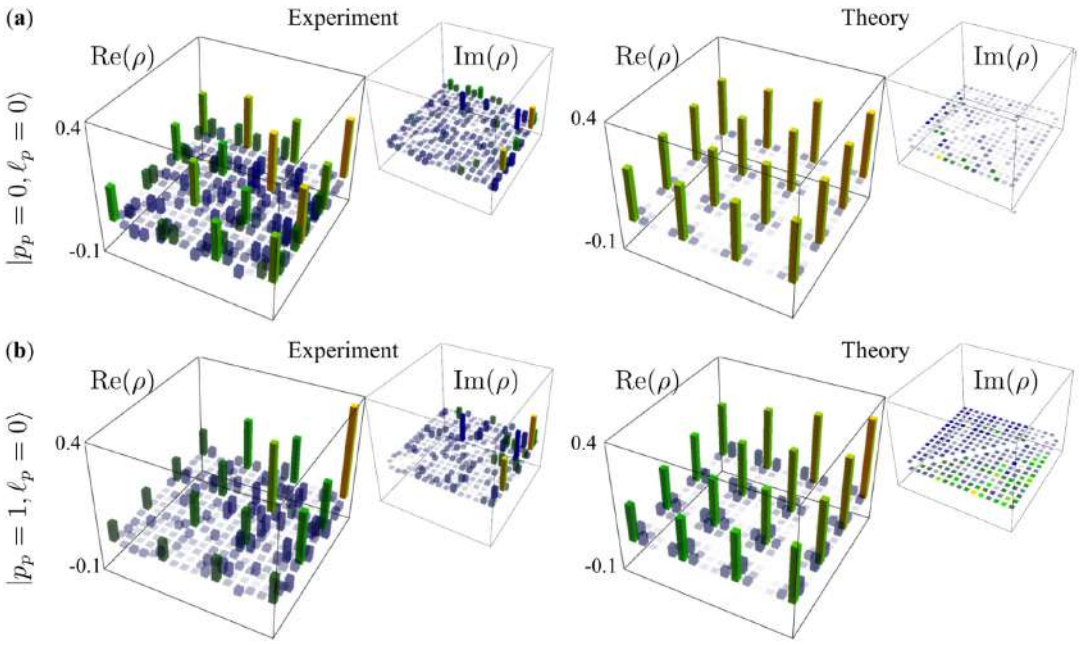

Figure 3.1: State tomography for the OAM subspace. Experimental and theoretical plots of the bi-photon density matrix in an OAM subspace ($l_i = -l_s = 1$) for the LG pump beam with $l_p = 0$ and (a) $p_p = 0$ and (b) $p_p = 1$. We considered the subspace spanned by radial values of p_s and p_i going from 0 to 3. Taken from Ref. [65].

radial mode space [65], and up to 26 in a 43-dimensional radial and azimuthal space using an intensity-flattening technique [66], as shown in figures 3.1 and 3.2, respectively. In Figure 3.1 the down-converted state is generated tailoring the pump beam in a superposition of different LG-modes. After projection of the state, the entangled photons are reconstructed using tomography. The top and bottom rows show the experimental and theoretical results of the density matrix in the subspace spanned by OAM values $l_i = -l_s = 1$, and radial values p_s and p_i from 0 to 3. Using a LG pump beam with (a) $l_p = 0$ and $p_p = 0$, and in (b) with $l_p = 0$ and $p_p = 1$.

Figure 3.2 shows the full LG-mode entanglement in a 43-dimensional subspace. It also describes that measurements in multiple LG mutually unbiased bases (MUBs) can signifi-

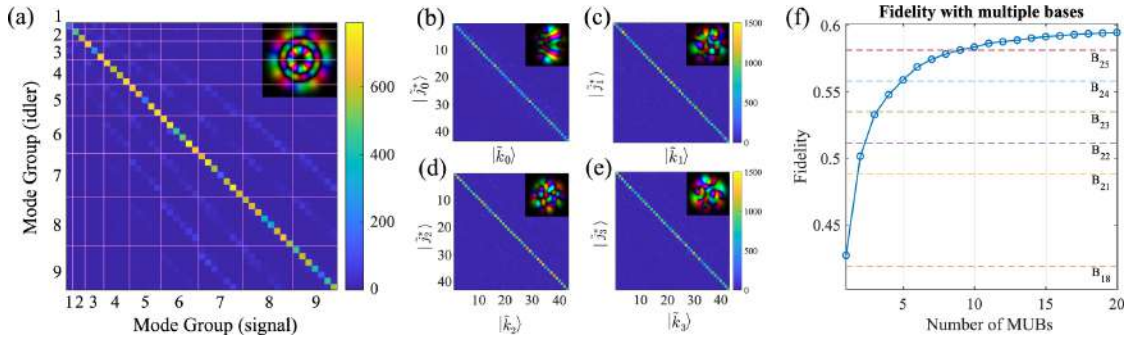

Figure 3.2: Full LG-mode entanglement in a 43-dimensional subspace. (a) Two-photon coincidence counts showing correlations in the standard LG basis of radial and azimuthal modes belonging to nine different mode groups (indicated by the pink lines). (b)–(e) Two-photon coincidence counts showing correlations in the first four mutually unbiased bases (LG MUBs) with respect to the standard basis. Correlations in 21 mutually unbiased bases allow us to lower bound the fidelity of our state to a maximally entangled state, and certify an entanglement dimensionality of $d_{ent} = 26$. The advantage of using measurements in more LG MUBs is shown in (f), where the estimated fidelity allows us to violate higher dimensionality bounds (B_{dent-1}), thus allowing us to certify higher entanglement dimensionality as the number of MUBs used increases. Taken from Ref. [65].

cantly increase the noise-robustness of high-dimensional entanglement certification. MUBs are fully equivalent basis (to the LG basis) that can be use to describe the entangled state. Measurements in one basis do not provide any information about possible results in another basis, thus they are mutually unbiased. Figure 3.2(a) shows the full correlations of the down-converted state in the LG basis. The pink lines represent nine different groups of the radial and azimuthal modes. Examining the modes in relation to their mode group (a pink square on the plot), there is not much cross-talk between them. Experimental imperfections, however, produce cross-talk between adjacent mode groups (adjacent pink squares) $Mode\,Group\,idler = Mode\,Group\,signal \pm 1$. Figure 3.2(b) shows the correlations in the first four MUBs. Figure 3.2(f) shows the fidelity as a function of MUBs. This method enables the violation of higher dimensionality bounds B_{dent-1}, and certify high-dimensional entanglement.

To achieve these high-dimensional radial spaces and beyond, we need first to spatially characterize the quantum space. SPDC-generated entangled photon pairs have traditionally been used for this purpose. The photon's degrees of freedom make it a natural candidate for studying high-dimensional entanglement in nature and they can also be easily manipulated in a laboratory setting. To the best of our knowledge, the first attempt to characterize and measure the radial correlations of down-converted LG-modes was done by Miatto et al. [67] and Salakhutdinov et al. [68], respectively. Figure 3.3 (from Ref. [68]) shows the radial quantum correlations with a good agreement between theory and experiment. The horizontal and vertical axes represent the signal and the idler radial modes, p_s and p_i, respectively. The color code describes the coincidence counts rates, being red the highest rates, and dark blue the lowest rates. It also illustrates that the smaller the detection-mode waist w (which is related to the pump beam waist through the ratio $\gamma = w_p/w$), the less cross-correlated terms (the off-diagonal elements in the density matrix). These results of characterize and measure radial correlations with negligible cross-correlations demonstrate that the radial degree of freedom in the transverse profile of down-converted photons is a useful entanglement resource upon fine-tuning of the pump and detected mode waists.

Other studies have explored the quantum nature of the radial number presenting interesting insights through Hong-Ou-Mandel (HOM) interference [69], and operator formalism applying traditional and non-traditional methods such as group theory based on Lie algebra [70] and differential-operator formalism [71]. From these investigations we know that the LG-radial index is a quantum number. So, together with the OAM index could significantly increase the information capacity per single photon. In Ref. [69] the quantum test of the radial degree of freedom was performed using two-photon interference in a beam splitter. Figure 3.4(a) shows the indistinguishability between the two photons through the

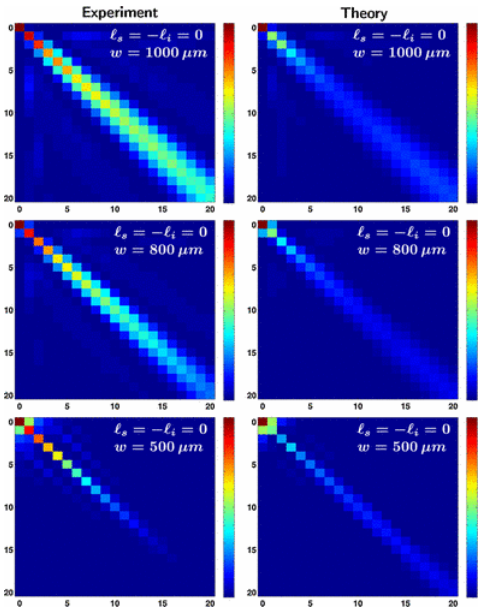

Figure 3.3: Quantum correlations between radial modes with differen p for ($l_s = l_i = 0$). Shown are the normalized (divided by maximum) coincidence count rates (colorcoded) as a function of the radial-mode numbers p_s (horizontal axis) and p_i (vertical axis) of the detection modes. Different rows depict results for different detection-mode waists as indicated. Left column, experimental data; right column: theoretical prediction. It is clearly visible that the smaller the detection-mode waist gets, the smaller the off-diagonal counts will be. This is a sign that we approach the Schmidt basis for $\gamma \to \gamma^*$. The detection-mode waists corresponds to waist ratios of (from top to bottom) $\gamma = 2.4$, 3, 4.9; see [67]. Taken from Ref. [68], with copyright permission from the journal.

characteristic dip of the HOM effect. Figure 3.4(b) shows the HOM coalescence pick, which is used to verify the interference effect. The coalescence enhancement test is less affected by experimental imperfections as compared to HOM interference. In Ref. [70], the authors establish a connection between the operator of a two-dimensional harmonic oscillator in cylindrical coordinates and the radial index of LG-modes. They also find that the action of the displacement operator on the fundamental mode results in a radial coherent state with fixed l. The probability distribution of the radial coherent state is given by

$$\begin{aligned} W_p &= |\langle p, l|\zeta\rangle|^2 \\ &= \frac{(|l|+1)^{|l|+1}(p+|l|)!}{p!|l|!}\frac{\bar{p}^p}{(\bar{p}+|l|+1)^{p+|l|+1}}, \end{aligned} \tag{3.1}$$

where $|\zeta\rangle$ is a radial coherent state described by

$$|\zeta\rangle = \hat{D}(\xi)|k,k\rangle. \tag{3.2}$$

The average number of rings is written as

$$\bar{p} = \frac{|\zeta|^2}{|\zeta|^2-1}(|l|+1). \tag{3.3}$$

Figure 3.5 shows the probability distribution of a radial coherent state with fixed l. The x and y axes represent the radial number p and the average number of rings $\bar{p}$.

On the other hand, Plick et al. [71] explained the meaning of the radial quantum number in terms of the intrinsic hyperbolic momentum charge through differential operator formalism in both the paraxial coordinate representation (position) and the exact momentum space representation. They derive a general differential operator for any value of z given by

$$\widehat{N}_z = -\frac{\hbar w_z^2}{8}\nabla_t^2 - \frac{z}{kw_0^2}\widehat{P}_H - \frac{\widehat{L}_z}{2} + \frac{\hbar}{2}\left(\frac{r^2}{w_0^2}-1\right), \tag{3.4}$$

and identify the four terms of this operator with physical parameters. They conclude that the radial degree of freedom arises from $\widehat{P}_H$, which is the hyperbolic momentum operator

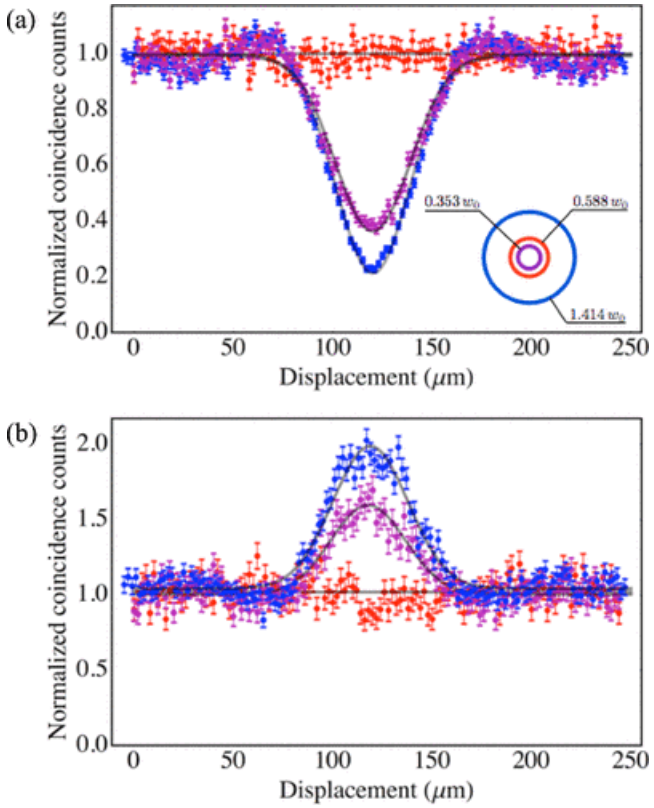

Figure 3.4: (a) Experimental data of the Hong-Ou-Mandel interference in the radial DOF (coincidence detection with D_A and D_B): The HOM dip indicates indistinguishability between the two photons; the flat data (red) corresponds to two completely distinguishable radial states, while the other two curves (magenta and blue) correspond to a pair of partially distinguishable and indistinguishable radial states. The visibilities of the dips are $V = 0.014 \pm 0.027$, $V = 0.465 \pm 0.030$, and $V = 0.646 \pm 0.026$, respectively. The inset shows that the radius of each holographic kinoform displayed on the SLM-B which determined the value of the distinguishability. (b) Experimental data of the Hong-Ou-Mandel coalescence enhancement (coincidence detection with D_B and $D_{B'}$); the enhancement increases for indistinguishable photons in the radial DOF. The enhancements due to coalescence are $C = 1.113 \pm 0.093$, $C = 1.590 \pm 0.060$, and $C = 1.907 \pm 0.047$, respectively. The error bars correspond to one standard deviation and were calculated from a Poisson distribution. Solid curves are the best theoretical Gaussian fit. Note that the normalization factor for (a) and (b) are different. Taken from Ref. [69], with copyright permission from the journal.

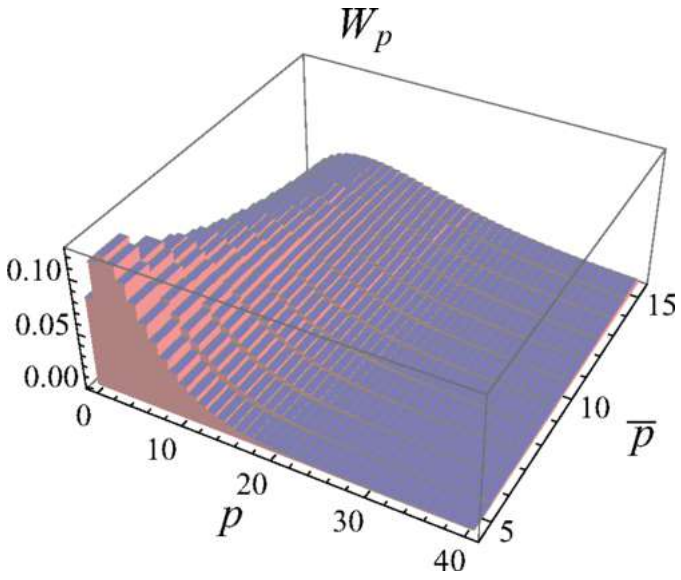

Figure 3.5: Probability distribution W_p for a coherent state $|\zeta\rangle$ with $l = 1$ as a function of p and the ring average number $\bar{p}$. Taken from Ref. [70], with copyright permission from the journal.

that generates dilation. The other three terms are related to the beam parameters that influence, but are not influenced by the radial mode. Hence, to define the radial index requires precise propagation distance (z), OAM (l), and beam width (w_0) measurements. Figure 3.6 represents the expectation value of the hyperbolic momentum as a function of the propagation distance for several values of the radial index n. Looking at the different colors we can see that the scaling is linear, and cross the origin where the beam waist takes its smallest value.

Clearly, the aforementioned results do not include all the scientific studies on radial quantum numbers of Laguerre-Gauss modes. Nevertheless, the purpose of this brief review is to illustrate some of the insightful results that have been achieved by taking a closer look at the forgotten radial index. We refer the interested reader to the referenced articles and references therein.

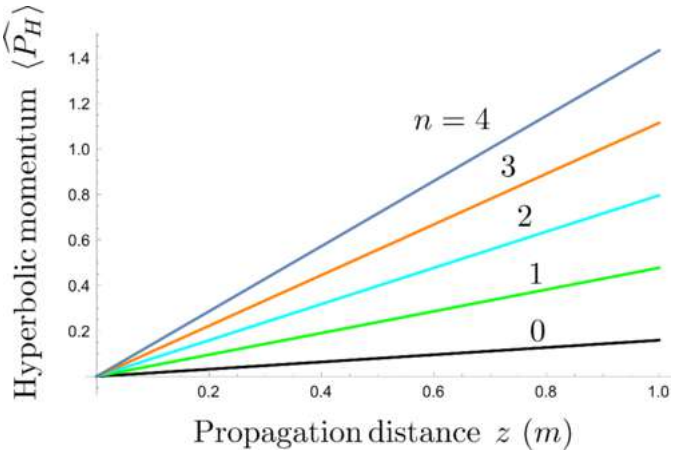

Figure 3.6: Expectation value of the hyperbolic momentum as a function of propagation distance for five different values of the radial index. In all cases the scaling is linear, passing through the origin where the beam waist is smallest. Note that this does not include the prefactor of $-z/kw_0^2$ in Eq. (3.4). For that whole term together the z scaling is quadratic, which, in the far field, is equivalent to the scaling of the Laplacian term. Note that the hyperbolic momentum is scale invariant and thus unitless. Taken from Ref. [71], with copyright permission from the journal.

3.2 Generation of entangled radial N00N states

In Ch. II we discussed that photon pairs generated by SPDC processes are entangled in the spatial degree of freedom, and LG modes are the most commonly used basis to describe the single-photon mode spaces. Hereafter in this chapter, we only consider the radial component p of the optical fields namely the pump and SPDC beams. We also consider that the other quantum numbers are identical, and in particular we take $l = 0$. Therefore, from the results of Sec.(2.3) in the form of Eqs. (2.46), (2.47) and (2.48), we have that the state of a pump that is put into a superposition of pure radial LG modes is given by

$$|\mathrm{P}_{\mathrm{pump}}\rangle = \sum_{p_\mathrm{p}} a_{p_\mathrm{p}} \, |p_\mathrm{p}\rangle, \tag{3.5}$$

where a_{p_p} are complex amplitudes and $\sum_{p_\mathrm{p}} |a_{p_\mathrm{p}}|^2 = 1$. So for that case we have that the radial entangled state can be rewritten as

$$|\psi_{\mathrm{SPDC}}\rangle = \sum_{p_s} \sum_{p_i} C_{p_s,p_i} \, |p_s\rangle |p_i\rangle, \tag{3.6}$$

where

$$C_{p_s,p_i} = \sum_{p_\mathrm{p}} a_{p_\mathrm{p}} \, B_{p_\mathrm{p};\, p_s,p_i}. \tag{3.7}$$

These are the *full* coincidence *radial* amplitudes, where $B_{p_\mathrm{p};\, p_s,p_i}$ are the coincidence amplitudes given by Eq. (2.45), calculated for each *individual* radial component $|p_\mathrm{p}\rangle$ of the initial pump. For simplicity, we omit the superscript $l = 0$ in the description of radial states.

The working principle for the generation of MES with radial modes is to tailor the pump beam with particular superpositions of radial modes to generate a target state. Then we have to calculate the full coincidence amplitudes of the entangled state. If we chose the right superposition for the pump beam, this is both the number of modes and their weights, the down-converted state will be a maximally-entangled-state within their radial modes.

As a first example we would like to generate the two-dimensional maximally entangled radial state

$$|\psi\rangle = \frac{1}{\sqrt{2}}(|01\rangle + |10\rangle). \tag{3.8}$$

So, we consider a pump that has been tailored into a superposition of two radial modes given by

$$|\mathrm{P}_{\mathrm{pump}}\rangle = \frac{1}{\sqrt{2}} \left(|1\rangle + |2\rangle\right). \tag{3.9}$$

Then we calculate the individual probability amplitudes $B_{p_\mathrm{p};\, p_s,p_i}$ for each individual radial component of the pump. This is followed by calculating the full coincidence amplitudes. So

we have

$$\begin{aligned} C_{p_s,p_i} &= \sum_{p_\mathrm{p}=1}^{2} a_{p_\mathrm{p}}\, B_{p_\mathrm{p};\,p_s,p_i} \\ &= a_1\, B_{1;\,p_s,p_i} + a_2\, B_{2;\,p_s,p_i} \\ &= \frac{1}{\sqrt{2}}\left(B_{1;\,p_s,p_i} + B_{2;\,p_s,p_i}\right), \end{aligned} \tag{3.10}$$

where

$$B_{p_\mathrm{p};p_s,p_i} = \int_0^{2\pi} \mathrm{d}\phi \int_0^{\infty} \rho\, \mathrm{d}\rho\, \mathrm{LG}_{p_\mathrm{p}}(\rho,\phi)[\mathrm{LG}_{p_s}(\rho,\phi)]^*[\mathrm{LG}_{p_i}(\rho,\phi)]^* \tag{3.11}$$

with $p_\mathrm{p} = \{1, 2\}$. As a result, the radial down-converted state is given by

$$\begin{aligned} |\psi_{\mathrm{SPDC}}\rangle &= \sum_{p_s}\sum_{p_i} C_{p_s,p_i}\, |p_s\rangle|p_i\rangle \\ &= \sum_{p_s}\sum_{p_i} \frac{1}{\sqrt{2}}\left(B_{1;\,p_s,p_i} + B_{2;\,p_s,p_i}\right)|p_s\rangle|p_i\rangle, \end{aligned} \tag{3.12}$$

which contains a two-dimensional radial MES. Figure 3.7 shows the resulting coincidence amplitudes or density matrix $|C_{p_s,p_i}|^2 = \langle\psi_{\mathrm{SPDC}}|\psi_{\mathrm{SPDC}}\rangle$ as a function of the signal and idler radial modes, p_s and p_i, respectively. Note that the two-dimensional radial MES is given by the elements shown in red. The other amplitudes constitute unwanted noise.

To generate the three-dimensional radial MES

$$|\psi'\rangle = \frac{1}{\sqrt{3}}\left(|00\rangle + |01\rangle + |10\rangle\right), \tag{3.13}$$

we first take into account a pump beam put into a superposition of three radial modes with identical complex amplitudes ($a_{p_\mathrm{p}} = 1$)

$$|\mathrm{P}'_{\mathrm{pump}}\rangle = \frac{1}{\sqrt{3}}\left(|0\rangle + |1\rangle + |2\rangle\right). \tag{3.14}$$

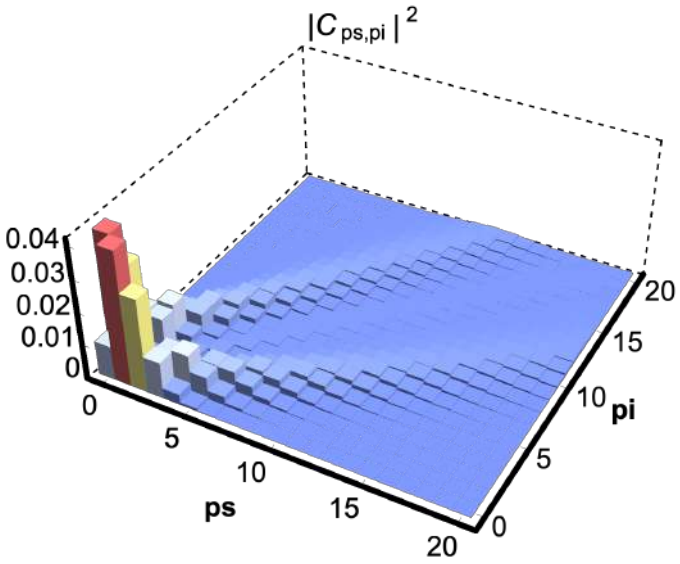

Figure 3.7: Spatial spectrum distributions of a two-dimensional radial maximally entangled state (MES). The x and y axes are the signal p_s and idler p_i radial values of the photon pair. The z axis shows the coincidence probability amplitudes $|C_{p_s,\,p_i}|^2$. The amplitudes in red constitute the target state: $|\psi\rangle = (|11\rangle + |22\rangle)/\sqrt{2}$, and the other components are unwanted noise.

Thus, following the aforementioned steps, the down-converted state is given by

$$\begin{aligned} |\psi^{'}_{\text{SPDC}}\rangle &= \sum_{p_s}\sum_{p_i} C^{'}_{p_s,p_i}\,|p_s\rangle|p_i\rangle \\ &= \sum_{p_s}\sum_{p_i} \frac{1}{\sqrt{3}}\left(B^{'}_{0;\,p_s,p_i} + B^{'}_{1;\,p_s,p_i} + B^{'}_{2;\,p_s,p_i}\right)|p_s\rangle|p_i\rangle. \end{aligned} \tag{3.15}$$

The resulting probability amplitudes of the generated down-converted state are shown in Figure 3.8a as a function of the signal and idler radial modes, p_s and p_i, respectively. Note that the three-dimensional radial MES is given by the elements shown in red and yellow. The other amplitudes constitute unwanted noise.

If we look at Figure 3.8a we can see that this is not a three-dimensional MES. To generate such a state we need to increase the two smaller amplitudes of the down-converted

states $|01\rangle$ and $|10\rangle$ shown in yellow. This can be accomplished by increasing the pump mode amplitudes of the states $|1\rangle$ and $|2\rangle$.

Mathematically, we have the pump state

$$|\mathrm{P}''_{\mathrm{pump}}\rangle = \frac{1}{2}\left(|0\rangle + \sqrt{1.5}\,|1\rangle + \sqrt{1.5}\,|2\rangle\right). \tag{3.16}$$

So that the entangled state becomes

$$\begin{aligned}|\psi''_{\mathrm{SPDC}}\rangle &= \sum_{p_s}\sum_{p_i} C''_{p_s,p_i}\,|p_s\rangle|p_i\rangle \\ &= \sum_{p_s}\sum_{p_i}\frac{1}{2}\left(B''_{0;\,p_s,p_i} + B''_{1;\,p_s,p_i} + B''_{2;\,p_s,p_i}\right)|p_s\rangle|p_i\rangle. \end{aligned}\tag{3.17}$$

These coincidence amplitudes are depicted in Figure 3.8b. As we can see the entangled state is not a MES yet. Thus we continue increasing the amplitude of the pump modes.

This time we set the pump mode amplitudes a_{p_1} and a_{p_2} equals to $\sqrt{2.25}$ to get the pump state

$$|\mathrm{P}'''_{\mathrm{pump}}\rangle = \frac{1}{\sqrt{5.5}}\left(|0\rangle + \sqrt{2.25}\,|1\rangle + \sqrt{2.25}\,|2\rangle\right). \tag{3.18}$$

Therefore the down-converted state can be written as

$$\begin{aligned}|\psi'''_{\mathrm{SPDC}}\rangle &= \sum_{p_s}\sum_{p_i} C'''_{p_s,p_i}\,|p_s\rangle|p_i\rangle \\ &= \sum_{p_s}\sum_{p_i}\frac{1}{\sqrt{5.5}}\left(B'''_{0;\,p_s,p_i} + B'''_{1;\,p_s,p_i} + B'''_{2;\,p_s,p_i}\right)|p_s\rangle|p_i\rangle. \end{aligned}\tag{3.19}$$

The resulting coincidence amplitudes are shown in Figure 3.8c as a function of the signal and idler radial modes, p_s and p_i, respectively. Note that the generated entangled state is a three-dimensional MES given by the elements shown in red. The other amplitudes constitute unwanted noise.

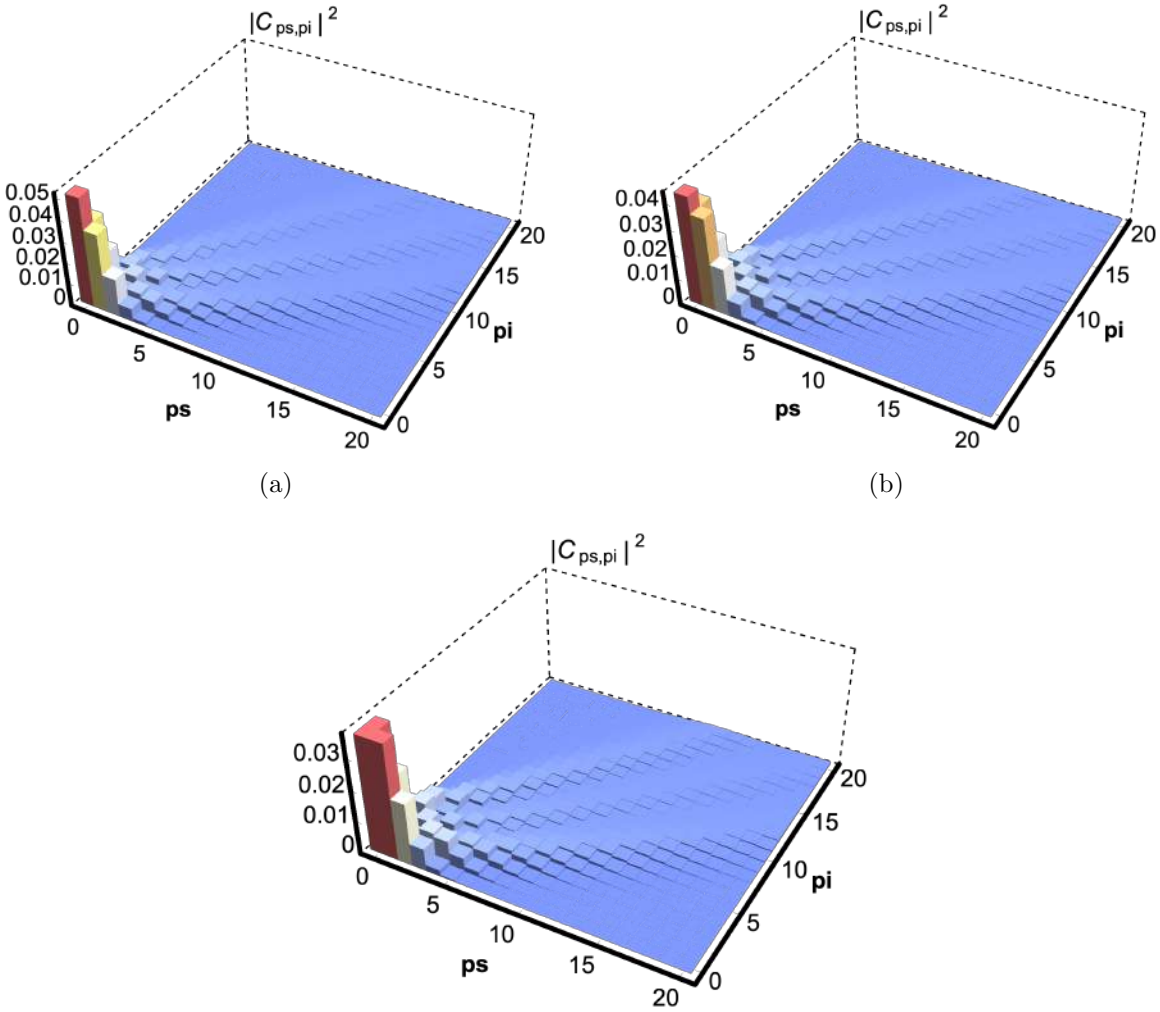

Figure 3.8: Spatial spectrum distributions of three-dimensional radial entangled states. (a)-(c) The spatial spectrum distribution for the input beam put into the superposition $1/\sqrt{3}(|0\rangle + |1\rangle + |2\rangle)$, $1/2(|0\rangle + \sqrt{1.5}\,|1\rangle + \sqrt{1.5}\,|2\rangle)$ and $1/\sqrt{5.5}(|0\rangle + \sqrt{2.25}\,|1\rangle + \sqrt{2.25}\,|2\rangle)$, respectively. (c) Three-dimensional radial maximally entangled state (MES). Those amplitudes in red constitute the target state: $|\psi^{'}\rangle = (|00\rangle + |01\rangle + |10\rangle)/\sqrt{3}$, while the other components are unwanted noise. The x and y axes are the signal p_s and idler p_i radial values of the photon pair. The z axis shows the coincidence probability amplitudes $|C_{p_s,p_i}|^2$.

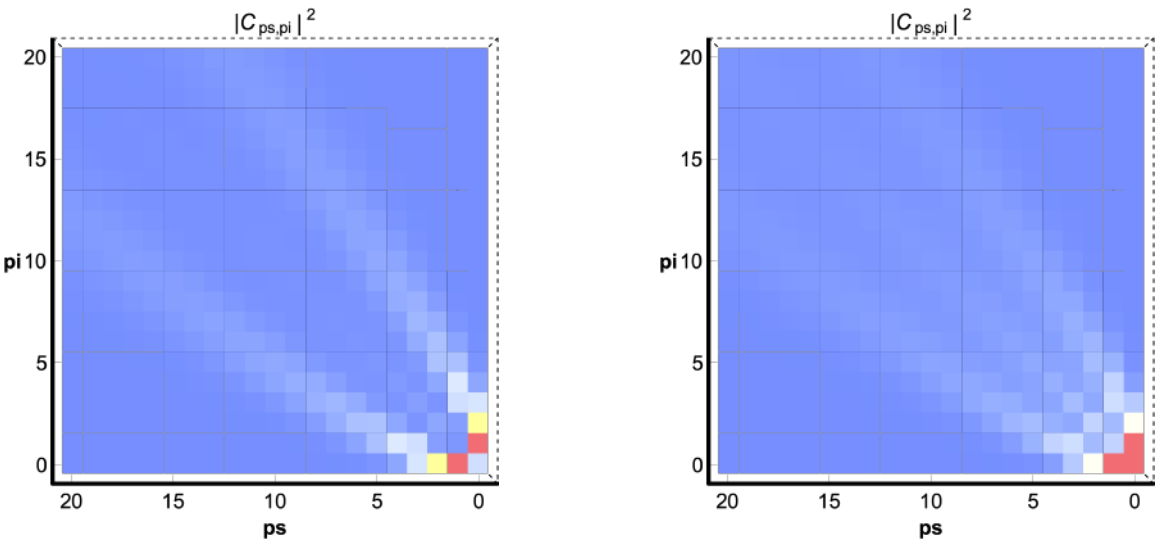

(a) 2D MES

(b) 3D MES

Figure 3.9: Radial forks of the two-dimensional and three-dimensional maximally-entangled-states (MES), (a) and (b) respectively. If we neglect the very-low amplitudes ($\sim 10^{-6}$ and lower, shown in dark blue) is clear to see that the number of "tines" on the radial-fork increases with the dimensionality.

In the method presented in this chapter for the generation of radial MES, even if we neglect the very-low amplitudes those of the order of 10^{-6} and lower (shown in dark blue in the figures) we still have a lot of unwanted noise. This looks clear if we look at the plots from a two-dimensional point of view as shown in Figure 3.9. In this figure we can see (neglecting the very-low dark blue amplitudes) two and three main diagonals for the two-dimensional and three-dimensional radial MES, respectively. We call them *radial forks*. We find that the number of tines on the fork increases with the dimensionality of the MES. This indicates the need for a better optimization process that controls the pump amplitudes according to down-converted target states. Additionally, there is the problem of finding a reliable norm function since the problem gets more complex as we go to higher dimensions. We elaborate in Ch. VII.

In this chapter we presented a method for the generation of maximally-entangled-states (MES) with Laguerre-Gauss radial modes. Nevertheless, since these states are noisy in nature, cross correlations between their eigenstates $|p_s, p_i\rangle$ are expected, and this limits their generation. Another limitation is the optimization process needed as we discuss in Ch. VII. In the cases presented here, all the choices were made by inspection, so the next step would be to optimize the weights (amplitudes) of the superposition of the input pump.

CHAPTER IV

PROTOCOL FOR HYPERENTANGLEMENT GENERATION BASED ON INTERFERENCE AND DETECTION-BASIS CONTROL

4.1 The Hong-Ou-Mandel effect

Two-photon interference or Hong-Ou-Mandel (HOM) interference is an essential element of quantum technologies such as quantum gates and quantum repeaters [14, 72]. HOM interference is a method to quantify the two-photon interference at a beam splitter when considering two indistinguishable photons incident at each input-port of a symmetric beam splitter. This two-photon interference at a beam splitter exhibits the photon bunching effect attributed to their Bosonic nature in which indistinguishable photons go together to either output-port of the beam splitter [59].

Let's describe HOM interference in detail. To start assume two distinguishable photons by polarization are incident to each input-port of a 50:50 beam splitter, so the initial state is given by

$$|\psi_{\text{in}}\rangle = \hat{a}_H^\dagger \hat{b}_V^\dagger |0\rangle, \tag{4.1}$$

where $a_H^\dagger$ and $\hat{b}_V^\dagger$ are the creation operators corresponding to the modes of horizontally polarized light in input-port a and vertically polarized light in input-port b, respectively, and $|0\rangle = |0\rangle_a|0\rangle_b|0\rangle_c|0\rangle_d$ is the vacuum state. The operators of each of these fields must satisfy the bosonic commutation relations

$$\left[\hat{a}_i, \hat{a}_j^\dagger\right] = \delta_{ij}, \quad [\hat{a}_i, \hat{a}_j] = 0 = \left[\hat{a}_i^\dagger, \hat{a}_j^\dagger\right]; \quad i, j = 1, 2, 3, \tag{4.2}$$

where $\hat{a}_i$ and $\hat{a}_j$ represent electromagnetic fields in mode i and j, respectively. For input modes a and b, and output modes c and d in a beam splitter we use the notation $\hat{a}$, $\hat{b}$ and $\hat{c}$, $\hat{d}$ to represent annihilation operators in that modes.

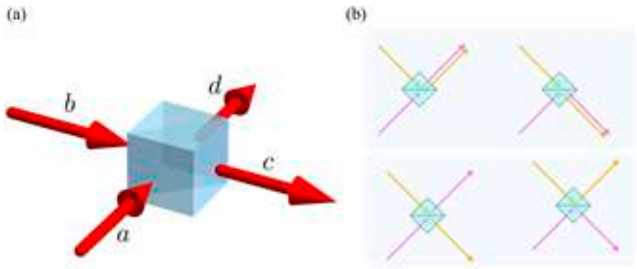

Figure 4.1: Action of a beam splitter. (a) Beam splitter with input ports labeled a and b, and output ports labeled c and d. Arrows indicate the field propagation directions. (b) The four ways the two photons can exit from the beam splitter–through the same port (top row) or different ports (bottom row). Taken from Ref. [73], with copyright permission from the journal.

After beam splitter transformations

$$\hat{a} = \frac{1}{\sqrt{2}}\left(\hat{c} - i\hat{d}\right), \tag{4.3}$$

$$\hat{b} = \frac{1}{\sqrt{2}}\left(-i\hat{c} + \hat{d}\right), \tag{4.4}$$

the output state is given by

$$\begin{aligned} a_H^\dagger \hat{b}_V^\dagger |0\rangle &\xrightarrow{BS} \frac{1}{2}\left(\hat{c}_H^\dagger + i\hat{d}_H^\dagger\right)\left(i\hat{c}_V^\dagger + \hat{d}_V^\dagger\right)|0\rangle \\ &= \frac{1}{2}\left(i\hat{c}_H^\dagger\hat{c}_V^\dagger + \hat{c}_H^\dagger\hat{d}_V^\dagger - \hat{d}_H^\dagger\hat{c}_V^\dagger + i\hat{d}_H^\dagger\hat{d}_V^\dagger\right)|0\rangle. \end{aligned} \tag{4.5}$$

Note that under these considerations we obtain all the classical expected outcomes. The first and last terms represent that the two photons are going together through the same output-port of the beam splitter, and the second and third terms show the two photons leaving the beam splitter separately through different output-ports. This behavior is illustrated in Figure 4.1(b). On the top row the two photons exit the beam splitter through the same port, and on the bottom row they exit through different ports. Figure 4.1(a) illustrates the input and output ports labels, a and b, and c and d, respectively. The red arrows indicate the propagation direction of the fields.

Now let's consider identical photons coming in the beam splitter. So that from Eq. (4.5) the output state becomes

$$\begin{aligned} a_H^\dagger \hat{b}_V^\dagger |0\rangle \quad &\xrightarrow{BS} \quad \frac{1}{2}\left(i\hat{c}^\dagger\hat{c}^\dagger + \underbrace{\hat{c}^\dagger\hat{d}^\dagger - \hat{d}^\dagger\hat{c}^\dagger}_{=0} + i\hat{d}^\dagger\hat{d}^\dagger \right)|0\rangle \\ &= \quad \frac{i}{2}\left(\left(\hat{c}^\dagger\right)^2 + \left(\hat{d}^\dagger\right)^2 \right)|0\rangle \\ &= \quad \frac{i}{\sqrt{2}}\left(|2\rangle_c + |2\rangle_d\right). \end{aligned} \tag{4.6}$$

This result is the so-called HOM interference or two-photon interference effect in a beam splitter. We remark it is the overall two-photon states that interfere and not single photon states. If we place single photon detectors in each output-port they should never register coincidence counts. But when measuring the spatial correlations between the two overlapped photons, an interference pattern can be observed in the relative separation between them. This is achieved by changing the position of the beam splitter, or one of the path lengths of the photons. This path variation will introduce a slight nonzero time delay, and the photons independently will be reflected or transmitted through the beam splitter causing both detectors sometimes to fire within a short time of each other.

4.2 Hyperentanglement generation in the spatial degree of freedom

Following Ref. [44] closely, figure 4.2 shows a diagram of our proposed setup. We consider a laser that generates coherent light divided by a 50:50 beam splitter (not shown). P1 and P2 are the pumps to the nonlinear crystals, NLC1 and NLC2, respectively. The modes A, B, C and D are input modes to the device, originally all in the vacuum state.

The two nonlinear crystals, NLC1 and NLC2, are identical and placed in a non-colinear configuration. We examine both processes in the SPDC regime, i.e. each adds one photon each to the output modes. Entanglement between photon pairs A and B is generated in

the first nonlinear crystal (NLC1). The photon in mode A is used as a seed to the second crystal (NLC2). In other words, the signal beam generated by NLC1 is superposed and aligned with the signal beam generated by NLC2. In such a situation the signal photon from NLC1 can induce coherence without inducing emission [74–76]. Furthermore, since the seed to NLC2 is a weak field compared to the pump field, it is extremely unlikely to cause stimulated down-conversion, hence the down-conversion can be assumed to be totally spontaneous for all practical purposes [77].

After this point there are assumed to be four photons in the device (this is ensured by post-selection), two in mode A and one each in modes B and C. After that, modes A and D, and modes B and C are mixed (interfered) on 50:50 beam splitters. This interference is Hong-Ou-Mandel (HOM) interference, which exhibits the photon bunching effect attributed to their Bosonic nature in which indistinguishable photons go together to either output-port of the beam splitter [59]. The spatial structure must be the same for HOM interference, and we apply the beam-splitter transformations in each OAM mode individually. The final step of the procedure is to herald on specific OAM superpositions as described in detail below. The desired state is then produced between modes B and C.

Examining this process in detail we take as our input the vacuum state in modes A, B, C and D. Hence, the initial state of the process (icon zero on Fig. 4.2), before interaction with the nonlinear crystals, is given by

$$|\psi_0\rangle = |0\rangle = |0\rangle_A|0\rangle_B|0\rangle_C|0\rangle_D. \tag{4.7}$$

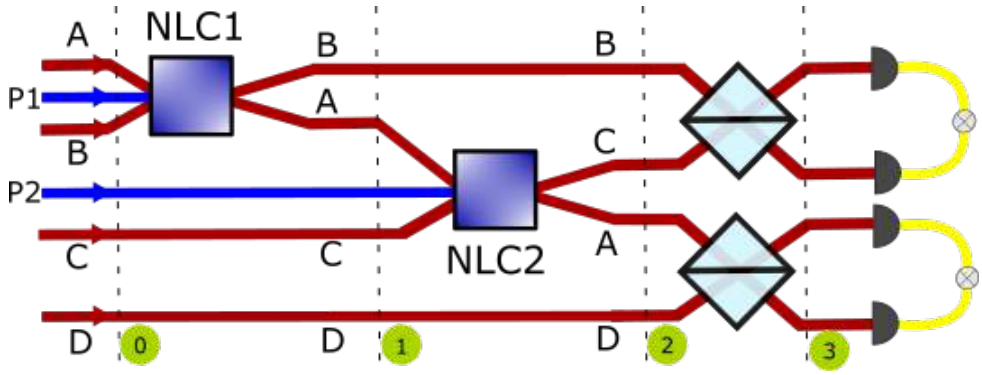

Figure 4.2: Conceptual diagram of the process. P1 and P2 are the pumps to the nonlinearities NLC1 and NLC2, respectively, each producing a down-converted pair of photons into the output modes. Entanglement between photon pairs A and B, generated in the first nonlinear crystal (NLC1), is linked to the remaining modes using the second nonlinear crystal (NLC2) in conjunction with the beam-splitters (light-blue boxes) that follow. A coincidence detection protocol using OAM detection-basis control is then used on modes A and D, heralding the desired state between modes B and C. The green icons represent the stages of evolution of the state as it moves through the device. Taken from Ref. [44], with copyright permission from the journal.

After interaction with the first nonlinear crystal (NLC1) the state of the system is described by (icon one on Fig. 4.2)

$$|\psi_1\rangle = \sum_l C_{\mathrm{AB}}^{-l,l}\, \hat{a}^\dagger_{-l} \hat{b}^\dagger_l\, |0\rangle, \tag{4.8}$$

where $C_{\mathrm{AB}}^{-l,l}$ are the coincidence amplitudes of the down-converted state, see Eq. (2.45), $\hat{a}^\dagger_{-l}$ and $\hat{b}^\dagger_l$ are the creation operators for the signal and idler modes, respectively, and for convenience we write the negative sign on the signal mode.

We now take the signal photon produced into the first nonlinear crystal (NCL1) and seed it into the down-conversion process of the second nonlinear crystal (NLC2). The state of the system after interaction with the second nonlinear crystal is then written as (icon

two on Fig. 4.2)

$$|\psi_2\rangle = \sum_{\mathcal{L}} \sum_{l} \gamma_{\mathrm{AC}}^{-\mathcal{L},\mathcal{L}}\, C_{\mathrm{AB}}^{-l,l}\, \hat{a}^{\dagger}_{-l} \hat{a}^{\dagger}_{-\mathcal{L}} \hat{b}^{\dagger}_{l} \hat{c}^{\dagger}_{\mathcal{L}} \,|0\rangle, \tag{4.9}$$

where $\gamma_{\mathrm{AC}}^{-\mathcal{L},\mathcal{L}}$ are the coincidence amplitudes of the down-converted state, see Eq. (2.45) and Eq. (2.48), and $\hat{a}^{\dagger}_{-\mathcal{L}}$ and $\hat{c}^{\dagger}_{\mathcal{L}}$ are the creation operators for the signal and idler modes, respectively.

After beam splitter transformations we have

$$|\psi_3\rangle = \sum_{\mathcal{L},l} \gamma_{\mathrm{AC}}^{\mathcal{L},-\mathcal{L}}\, C_{\mathrm{AB}}^{l,-l}\, (\hat{a}^{\dagger}_{l} - i\hat{d}^{\dagger}_{l})(\hat{a}^{\dagger}_{\mathcal{L}} - i\hat{d}^{\dagger}_{\mathcal{L}}) \times (\hat{b}^{\dagger}_{-l} - i\hat{c}^{\dagger}_{-l})(\hat{c}^{\dagger}_{-\mathcal{L}} - i\hat{b}^{\dagger}_{-\mathcal{L}})|0\rangle. \tag{4.10}$$

Expanding the products we have the state (icon three on Fig. 4.2)

$$\begin{aligned} |\psi_3\rangle = &\sum_{\mathcal{L},l} \gamma_{\mathrm{AC}}^{-\mathcal{L},\mathcal{L}}\, C_{\mathrm{AB}}^{-l,l}\, (\hat{a}^{\dagger}_{-l}\hat{a}^{\dagger}_{-\mathcal{L}} - i\hat{a}^{\dagger}_{-l}\hat{d}^{\dagger}_{-\mathcal{L}} - i\hat{d}^{\dagger}_{-l}\hat{a}^{\dagger}_{-\mathcal{L}} - \hat{d}^{\dagger}_{-l}\hat{d}^{\dagger}_{-\mathcal{L}}) \\ &\times (\hat{b}^{\dagger}_{l}\hat{c}^{\dagger}_{\mathcal{L}} - i\hat{b}^{\dagger}_{l}\hat{b}^{\dagger}_{\mathcal{L}} - i\hat{c}^{\dagger}_{l}\hat{c}^{\dagger}_{\mathcal{L}} - \hat{c}^{\dagger}_{l}\hat{b}^{\dagger}_{\mathcal{L}})\,|0\rangle. \end{aligned} \tag{4.11}$$

We can ensure we only have one photon each in modes A and D by heralding only on the coincidence between those two modes, so eliminating terms that do not have such coincidences, we obtain

$$|\psi_3\rangle = \sum_{\mathcal{L},l} \gamma_{\mathrm{AC}}^{-\mathcal{L},\mathcal{L}}\, C_{\mathrm{AB}}^{-l,l}\, (-i\hat{a}^{\dagger}_{-l}\hat{d}^{\dagger}_{-\mathcal{L}} - i\hat{d}^{\dagger}_{-l}\hat{a}^{\dagger}_{-\mathcal{L}}) \times (\hat{b}^{\dagger}_{l}\hat{c}^{\dagger}_{\mathcal{L}} - i\hat{b}^{\dagger}_{l}\hat{b}^{\dagger}_{\mathcal{L}} - i\hat{c}^{\dagger}_{l}\hat{c}^{\dagger}_{\mathcal{L}} - \hat{c}^{\dagger}_{l}\hat{b}^{\dagger}_{\mathcal{L}})\,|0\rangle. \tag{4.12}$$

Then, for clarity of notation we act these operators onto the vacuum kets ($|0\rangle$), resulting in

$$\begin{aligned} |\psi_3\rangle = &\sum_{\mathcal{L},l} \gamma_{\mathrm{AC}}^{-\mathcal{L},\mathcal{L}}\, C_{\mathrm{AB}}^{-l,l} (-i|-l\rangle_A|-\mathcal{L}\rangle_D - i|-\mathcal{L}\rangle_A|-l\rangle_D) \\ &\times (|l\rangle_B|\mathcal{L}\rangle_C - i|l,\mathcal{L}\rangle_B|0\rangle_C - i|0\rangle_B|l,\mathcal{L}\rangle_C - |\mathcal{L}\rangle_B|l\rangle_C), \end{aligned} \tag{4.13}$$

where $|l,\mathcal{L}\rangle_B|0\rangle_C$ represents two photons in mode B with OAM l and $\mathcal{L}$ and zero photons in mode C. Similarly, the state $|0\rangle_B|l,\mathcal{L}\rangle_C$ represents zero photons in mode B and two photons in mode C with OAM l and $\mathcal{L}$. The other states have one photon each.

4.3 Hyperentanglement generation using detection-basis control

This section follows Ref. [44] closely. In the experiment a coherent light beam is symmetrically split by a beam splitter, and illuminate the two identical nonlinear crystals, NLC1 and NLC2. Thus, photon pairs are created via SPDC; see Figure 6.1. As mentioned in the previous section, the signal beam (mode A) generated in NLC1, is superposed and aligned with the signal beam generated by NLC2. Then, the signal states in mode A and vacuum state in mode D, and idler states in modes B and C are mixed on 50:50 beam splitters. After that, we project modes B and C on the desired state using spatial light modulators (SLM). The SLM is programmed with a forked diffraction grating to specify the state into which the entangled state will be projected. After projection, the state is couple into single-mode fibers connected to a detector. This spatial filtering ensures that only the desired state will couple to the fiber, and a detector firing indicates a projection onto the desired state.

The desired state is produced between modes B and C by heralding on modes A and D in coincidence using state projectors on specific OAM superpositions. To project the modes B and C on the desired state we can use a process involving spatial light modulators (SLM), as mentioned.

In practice the multi-photon heralding of modes A and D may lead to unwanted quantum states in modes B and C, however, the production of multiple photon events is negligible due to the low conversion efficiency of the spontaneous process. For example, the probability to have one pair of photons is proportional to the square of the second-order nonlinear susceptibility $\chi^{(2)}$, while the probability to have two pairs is proportional to $(\chi^{(2)})^4$. For a BBO nonlinear crystal ($\chi^{(2)} \sim 10^{-12}\, m/V$) we have probabilities 10^{-24} and 10^{-48} for one

and two pairs, respectively. Hence unwanted four-photon events would account for $10^{-22}\%$ of the two-photon's total [78].

The key to this protocol is the choice of the projectors. It is important here to note that it is possible to project on *any superposition* of OAM modes up to an *arbitrarily-large* dimensionality. Any arbitrary superposition of OAM modes is itself a solution to the paraxial wave equation (due to linearity), and thus corresponds to a particular transverse field pattern. If we wish to project on such a mode we can create the inverse of this field pattern (for example with a spatial light modulator – SLM), and shine the photon on this pattern. If the incident photon has the desired field pattern then the inverse operation of the SLM will take it (and only it) to the fundamental Gaussian. If the photon is then shone on a single-mode fiber connected to a detector, then since only the fundamental will couple to the fiber, a detector firing indicates a projection onto programmed state.

It is important to note that in-principle phase and amplitude modulation is needed, though phase-only modulation could possibly be sufficient. Other experimental implementations allowing projecting on particular states exist as well [33,34,48,79].

Mathematically, we use the projector operators on modes A and D given over the general sums of the j and k modes

$$|P\rangle_D = \sum_j f_j^* |j\rangle_D, \tag{4.14}$$

$$|P\rangle_A = \sum_k g_k^* |k\rangle_A, \tag{4.15}$$

where (ignoring normalization constants) $|j\rangle_D = \hat{d}_j^\dagger |0\rangle_D$, $|k\rangle_A = \hat{a}_k^\dagger |0\rangle_A$ and, f_j^* and g_k^* are complex amplitudes. Hence the final state is given by

$$|\psi_f\rangle = {}_D\langle P|_A\langle P|\psi_3\rangle. \tag{4.16}$$

Substituting in the projector operators and the state $|\psi_3\rangle$ we have

$$\begin{aligned}|\psi_f\rangle =& \sum_{\mathcal{L},l} \gamma_{\mathrm{AC}}^{-\mathcal{L},\mathcal{L}}\, C_{\mathrm{AB}}^{-l,l} \sum_{j,k} f_j\, g_k\, ({}_D\langle j|_A\langle k|) \cdot (-i|-l\rangle_A|-\mathcal{L}\rangle_D - i|-\mathcal{L}\rangle_A|-l\rangle_D) \\ & \times (|l\rangle_B|\mathcal{L}\rangle_C - i|l,\mathcal{L}\rangle_B|0\rangle_C - i|0\rangle_B|l,\mathcal{L}\rangle_C - |\mathcal{L}\rangle_B|l\rangle_C). \end{aligned} \tag{4.17}$$

Then taking the inner product and simplifying we obtain

$$\begin{aligned}|\psi_f\rangle =& (-i) \sum_{\mathcal{L},l} \gamma_{\mathrm{AC}}^{-\mathcal{L},\mathcal{L}} C_{\mathrm{AB}}^{-l,l} \sum_{j,k} f_j g_k (\delta_{j,-\mathcal{L}}\delta_{k,-l} + \delta_{j,-l}\delta_{k,-\mathcal{L}}) \\ & \times (|l\rangle_B|\mathcal{L}\rangle_C - i|l,\mathcal{L}\rangle_B|0\rangle_C - i|0\rangle_B|l,\mathcal{L}\rangle_C - |\mathcal{L}\rangle_B|l\rangle_C). \end{aligned} \tag{4.18}$$

The entangled state described by Eq. (4.18) is a general state that allows the generation of low-dimensional and high-dimensional entangled states with orbital angular momentum (OAM).

Importantly, the dimensionality and structure of the entangled state $|\psi_f\rangle$ depends on the number of projector modes we choose and their amplitude values. This is what we call *detection-basis control*. In this expansion we can choose not only how many terms are in each superposition, but also the weights of all of those terms. The state-space produced is in principle infinite, and the experimenter is free to chose the size as they wish, or as large as the experimental parameters allow them. This presents both an opportunity and a problem. The opportunity is that it is a near certainty that many more states with desirable structures exist in higher dimensions beyond what we present here. The problem is that as dimensionality increases it becomes progressively-harder to search and find these states. This problem is further compounded by the fact that there are many ways to search for (and even define) entanglement. Also, some states that are entangled in very-many dimensions cannot be used as a resource for currently known protocols because they do not possess the necessary mathematical form (examples of states which do have this form are: mutually-unbiased-basis states, Bell states, N00N states, Greenberger–Horne–Zeilinger

states, etc.). Furthermore, the idea of "closeness" of quantum states becomes very muddy as dimensionality increases, and a state being close to a target entangled state does *not* generally mean that the state itself is strongly entangled itself. For further discussion of these points see chapters V and VII.

CHAPTER V

GENERATION OF N00N STATES WITH OAM AND TUNABLE DIMENSIONALITY

In this chapter we take the result of Sec. 4.2 in the form of equations (4.14), (4.15) and (4.18), and present several specific implementations (choices of the detection-basis control) and show that the state can be entangled in two and four dimensions, at minimum – and in a couple cases noiselessly. In each of the next three subsections we take progressively more projection modes and dimensions, one in section 5.1, two in section 5.2, three in section 5.3. We also show how particular choices of the weights in the mode expansions lead to entanglement in two modes or hyper-entanglement in four modes. Furthermore, to show the generality of the setup, we examine some other modes with more-complicated structures. Note that these values have been chosen "by inspection" without numerical optimization which is a highly-challenging prospect on its own. Throughout this chapter, we follow closely Ref. [44].

5.1 Generation of two-dimensional entangled OAM N00N states with single-mode projectors

To generate maximally entangled OAM states in two dimensions, we take into account projector operators with a single mode, $j \equiv k = -m$. So that equations (4.14) and (4.15) become

$$|P\rangle_D = f_m^*|-m\rangle_D, \tag{5.1}$$

$$|P\rangle_A = g_m^*|-m\rangle_A. \tag{5.2}$$

Since $j \equiv k = -m$, equation (4.18) transforms into

$$|\psi_{f1}\rangle = (-2i)\sum_{\mathcal{L},l} \gamma_{\mathrm{AC}}^{-\mathcal{L},\mathcal{L}} C_{\mathrm{AB}}^{-l,l} f_m g_m (\delta_{-m,-\mathcal{L}}\delta_{-m,-l}) \times (|l\rangle_B|\mathcal{L}\rangle_C - i|l,\mathcal{L}\rangle_B|0\rangle_C - i|0\rangle_B|l,\mathcal{L}\rangle_C - |\mathcal{L}\rangle_B|l\rangle_C), \tag{5.3}$$

which simplifies to

$$|\psi_{f1}\rangle = -2\gamma_{\mathrm{AC}}^{-m,m} C_{\mathrm{AB}}^{-m,m} f_m g_m \times (|m,m\rangle_B|0\rangle_C + |0\rangle_B|m,m\rangle_C). \tag{5.4}$$

Clearly, this is an OAM N00N state entangled in a two-dimensional space, which depends on the weights f and g of the OAM modes that we choose in the state projectors. Though the dimensionality of this state does not beat what can be done *without* the techniques in this paper we present it for completeness, to see how the dimensionality changes with various choices of the detection-basis.

5.2 Generation of two-dimensional entangled or four-dimensional hyperentangled OAM N00N states with two-mode projectors

To generate high-dimensional entangled OAM states, we first take into account projector operators with two modes, $j \equiv k$. Thus equations (4.14) and (4.15) become

$$|P\rangle_D = f_m^*|-m\rangle_D + f_n^*|-n\rangle_D, \tag{5.5}$$

$$|P\rangle_A = g_m^*|-m\rangle_A + g_n^*|-n\rangle_A. \tag{5.6}$$

The general equation described by Eq. (4.18) transforms into

$$\begin{aligned}|\psi_{f2}\rangle =& (-i)\sum_{\mathcal{L},l} \gamma_{\mathrm{AC}}^{-\mathcal{L},\mathcal{L}} C_{\mathrm{AB}}^{-l,l} [2 f_m g_m \delta_{-m,-\mathcal{L}}\delta_{-m,-l} + 2 f_n g_n \delta_{-n,-\mathcal{L}}\delta_{-n,-l} \\ &+ (f_m g_n + f_n g_m) \times (\delta_{-m,-\mathcal{L}}\delta_{-n,-l} + \delta_{-m,-l}\delta_{-n,-\mathcal{L}})] \\ &\times (|l\rangle_B|\mathcal{L}\rangle_C - i|l,\mathcal{L}\rangle_B|0\rangle_C - i|0\rangle_B|l,\mathcal{L}\rangle_C - |\mathcal{L}\rangle_B|l\rangle_C).\end{aligned} \tag{5.7}$$

Simplifying, we obtain

$$\begin{aligned}|\psi_{f2}\rangle =& -2[\gamma_{\mathrm{AC}}^{-m,m}C_{\mathrm{AB}}^{-m,m}f_m g_m(|m,m\rangle_B|0\rangle_C + |0\rangle_B|m,m\rangle_C) + \gamma_{\mathrm{AC}}^{-n,n}C_{\mathrm{AB}}^{-n,n}f_n g_n \\ &\times (|n,n\rangle_B|0\rangle_C + |0\rangle_B|n,n\rangle_C) + (\gamma_{\mathrm{AC}}^{-m,m}C_{\mathrm{AB}}^{-n,n}f_m g_n + \gamma_{\mathrm{AC}}^{-n,n}C_{\mathrm{AB}}^{-m,m}f_n g_m) \\ &\times (|n,m\rangle_B|0\rangle_C + |0\rangle_B|n,m\rangle_C)], \end{aligned} \tag{5.8}$$

which can be made a two-dimensional or four-dimensional entangled OAM state depending on the choice of amplitudes. To clarify, consider the case where all the amplitude values γs, Cs, fs and gs are equals to one. Thus the entangled state described by Eq. (5.8) simplifies to

$$\begin{aligned}|\psi_{f2}\rangle =& -2[|m,m\rangle_B|0\rangle_C + |0\rangle_B|m,m\rangle_C + |n,n\rangle_B|0\rangle_C + |0\rangle_B|n,n\rangle_C \\ &+ 2(|n,m\rangle_B|0\rangle_C + |0\rangle_B|n,m\rangle_C)]. \end{aligned} \tag{5.9}$$

Taking into account that we have two indistinguishable photons $|n,m\rangle = |m,n\rangle$, we may write the state as

$$\begin{aligned}|\psi_{f2}\rangle =& -2[|n,n\rangle_B|0\rangle_C + |0\rangle_B|n,n\rangle_C + (|m\rangle_B + 2|n\rangle_B)|m\rangle_B|0\rangle_C \\ &+ |0\rangle_B|m\rangle_C(|m\rangle_C + 2|n\rangle_C)]. \end{aligned} \tag{5.10}$$

The state displays several N00N-like partitions, the $|n,n\rangle$ part is a simple N00N state and a device tuned to detect those modes would see such a state with some other noise that is the result of the $|m\rangle$ modes. The state could also be seen as a N00N state between a pure $|m\rangle$ state and another state that is an unequal superposition of $|m\rangle$ and $|n\rangle$ states. In this case the $|n,n\rangle$ states would appear as noise. Hence, this state is mathematically entangled in at least two-dimensions to some degree depending on how it is partitioned and what states the detectors are tuned to.

If we take the amplitude values $f_m = 1$, $g_m = 1$, $f_n = 1$ and $g_n = -1$, the result is a four-dimensional hyper-entangled OAM N00N state

$$\begin{aligned} |\psi'_{f2}\rangle = &- 2[\gamma_{\mathrm{AC}}^{-m,m} C_{\mathrm{AB}}^{-m,m} (|m,m\rangle_B |0\rangle_C + |0\rangle_B |m,m\rangle_C) \\ &- \gamma_{\mathrm{AC}}^{-n,n} C_{\mathrm{AB}}^{-n,n} (|n,n\rangle_B |0\rangle_C + |0\rangle_B |n,n\rangle_C)], \end{aligned} \tag{5.11}$$

where the OAM modes m and n of two photons are entangled with the vacuum. The overall constants (the γ's and C's) may be chosen in tandem with the f's and g's such that they factor out. So we are left with a perfect, maximally-entangled, four-dimensional N00N state, and this is the most significant result. To the best of our knowledge, this is the current theoretical state of the art as we are not aware of any other setup that can produce a state that is both entangled to this high of a dimensionality and also in a state of high practical interest for the development of quantum technology.

So the dimensionality of the entangled state given by Eq. (5.8) depends on the amplitude values that we choose for f and g. With specific choices we can generate four-dimensional hyperentangled OAM N00N states and OAM entangled states in at least two-dimensions. The fact that the dimensionality of entangled state that this setup produces may be "tuned" may be of further theoretical and experimental interest.

5.3 Generation of complex hyperentangled OAM N00N states with three-mode projectors

To continue the investigation beyond our strongest result we now consider the case of projector operators with three modes. We provide this in order to show how the setup we propose can produce many different kinds of general states, and provides an excellent test-bed for research in high-dimensional entanglement. The projector modes in this case

are written as

$$|P\rangle_D = f_m^*|-m\rangle_D + f_n^*|-n\rangle_D + f_r^*|-r\rangle_D, \tag{5.12}$$

$$|P\rangle_A = g_m^*|-m\rangle_A + g_n^*|-n\rangle_A + g_r^*|-r\rangle_A. \tag{5.13}$$

So, plugging this in to Eq. (4.18) and performing a simple transformation we get

$$\begin{aligned}
|\psi_{f3}\rangle = &-2[\gamma_{\mathrm{AC}}^{-m,m} C_{\mathrm{AB}}^{-m,m} f_m g_m \times (|m,m\rangle_B|0\rangle_C + |0\rangle_B|m,m\rangle_C) + \gamma_{\mathrm{AC}}^{-n,n} C_{\mathrm{AB}}^{-n,n} f_n g_n \\
&\times (|n,n\rangle_B|0\rangle_C + |0\rangle_B|n,n\rangle_C) + \gamma_{\mathrm{AC}}^{-r,r} C_{\mathrm{AB}}^{-r,r} f_r g_r (|r,r\rangle_B|0\rangle_C + |0\rangle_B|r,r\rangle_C) \\
&+ (\gamma_{\mathrm{AC}}^{-m,m} C_{\mathrm{AB}}^{-n,n} f_m g_n + \gamma_{\mathrm{AC}}^{-n,n} C_{\mathrm{AB}}^{-m,m} f_n g_m)(|n,m\rangle_B|0\rangle_C + |0\rangle_B|n,m\rangle_C) \\
&+ (\gamma_{\mathrm{AC}}^{-m,m} C_{\mathrm{AB}}^{-r,r} f_m g_r + \gamma_{\mathrm{AC}}^{-r,r} C_{\mathrm{AB}}^{-m,m} f_r g_m)(|r,m\rangle_B|0\rangle_C + |0\rangle_B|r,m\rangle_C) \\
&+ (\gamma_{\mathrm{AC}}^{-n,n} C_{\mathrm{AB}}^{-r,r} f_n g_r + \gamma_{\mathrm{AC}}^{-r,r} C_{\mathrm{AB}}^{-n,n} f_r g_n)(|r,n\rangle_B|0\rangle_C + |0\rangle_B|r,n\rangle_C)].
\end{aligned} \tag{5.14}$$

The dimensionality of this state depends on the amplitude values that we choose for f and g. For example, taking the coincidence amplitudes γs and Cs equal to one, and then choosing the f's and g's equal to one, we obtain

$$\begin{aligned}
|\psi_{f3}\prime\rangle = &-2[(|m\rangle_B + 2|n\rangle_B)|m\rangle_B|0\rangle_C + |0\rangle_B|m\rangle_C(|m\rangle_C + 2|n\rangle_C) \\
&+ (|n\rangle_B + 2|r\rangle_B)|n\rangle_B|0\rangle_C + |0\rangle_B|n\rangle_C(|n\rangle_C + 2|r\rangle_C) \\
&+ (|r\rangle_B + 2|m\rangle_B)|r\rangle_B|0\rangle_C + |0\rangle_B|r\rangle_C(|r\rangle_C + 2|m\rangle_C)],
\end{aligned} \tag{5.15}$$

which contains several different terms that are non-separable (and potentially entangled). Specifically there are three N00N-like OAM states between both path and OAM, with the OAM modes being: $|m\rangle + 2|n\rangle$ (line 1), $|n\rangle + 2|r\rangle$ (line 2), and $|r\rangle + 2|m\rangle$ (lines 3). These modes are not mutually-orthogonal, each has some projection on to the other, so the state as a whole is not a six-dimensional N00N state – however since high-dimensional entanglement witnesses may be constructed from lower-dimensional partitions (as in [80]), such states

could exhibit high-dimensional entanglement, perhaps with some additional adjustment or optimization.

To continue to see how many different states can be produced by tuning this projectors, we set f's and g's equal to one with the exception of $g_r = -1$, the state given by Eq. (5.14) then becomes

$$\begin{aligned}|\psi''_{f3}\rangle = &-2[|n,n\rangle_B|0\rangle_C + |0\rangle_B|n,n\rangle_C + |r,r\rangle_B|0\rangle_C + |0\rangle_B|r,r\rangle_C \\ &+ (|m\rangle_B + 2|n\rangle_B)|m\rangle_B|0\rangle_C + |0\rangle_B|m\rangle_C(|m\rangle_C + 2|n\rangle_C)].\end{aligned} \tag{5.16}$$

Which again has a similar structure to Eq.5.16, with an important difference. In this case two of the OAM modes are mutually orthogonal – $|n,n\rangle$, and $|r,r\rangle$ – and the $|m\rangle + 2|n\rangle$ mode is orthogonal to $|r,r\rangle$. So it is clear that the fundamental structure of the output state can be significantly altered by choice of the weights that we choose for each mode on the state projectors $|P\rangle_D$ and $|P\rangle_A$ given by Eq. (5.12) and Eq. (5.13), respectively.

In cases where we do not achieve a perfect N00N state we do not quantify the amount of entanglement. This is because the quantification of entanglement in high dimensions is a difficult prospect (as we will discuss in the next section) and we provide these other states in order to stand in distinction to the ideal results, and also to show that the system is highly tunable which will motivate our future work into expanding to higher dimensions and optimizing the choice of weights. We elaborate in the following section.

CHAPTER VI

EXPERIMENTAL IMPLEMENTATION

6.1 Generation of beams carrying OAM and hyperentangled states

In this chapter we present the first steps towards the experimental implementation of our protocol "Generation of hyperentangled OAM N00N states". Our experimental setup is shown in Fig. 6.1, and consists of a pulsed Ti:Sapphire laser (Chameleon) centered at 810 nm, with a pulse width of 120 fs and a repetition rate of 80 MHz. An achromatic lens of focal length of 50 mm focuses the laser onto a 2-mm-thick BiBO crystal to achieve frequency doubling. The resultant sum frequency generation produces ≈220 mW of UV light at 405 nm. The remaining infrared light is eliminated using a shortpass filter which stop wavelengths $\lambda > 600$ nm, followed by a bandpass filter centered at 405 nm with 10 nm bandwidth, see element SBF in the figure. We use a lens of focal length 50 mm to collimate the up-converted light which is followed by a telescope composed of a lens of focal length 1000 mm and a lens of focal length 750 mm. This ensures a pump beam waist of 600 um at the crystals plane used for the down-conversion generation, BBO1 and BBO2. The three lenses are represented by element L1 on the diagram.

The generated entangled photon pairs by each BBO crystal are spectrally filtered by a long-pass filter with transmission wavelength $\lambda > 500$ nm, followed by a band-pass filter centered at 810 nm with 10 nm bandwidth, see element LBF on the diagram. In this way, we are certain that we are selecting photon pairs at 810 nm that are degenerate. Then all the photons are mixed on beam splitters. We use telescopes with a magnification of two to map each photon on spatial-light modulators (SLM) planes B, C, A and D. See elements

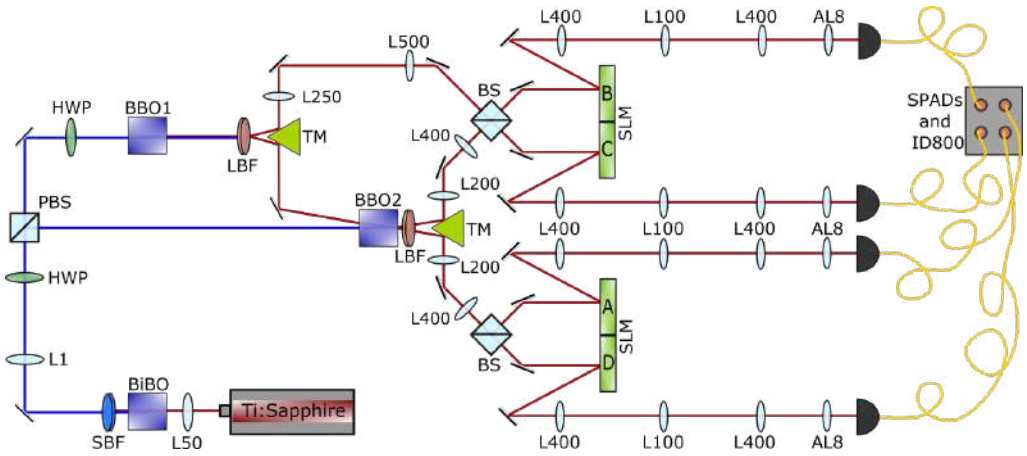

Figure 6.1: Experimental setup for the generation and detection of hyperentangled states. The first stage is the generation: the BiBO crystal is pumped by a Ti:Sapphire laser to produce UV light via second-harmonic generation. The first BBO crystal (BBO1) produces a down-converted photon pair, and BBO2 produces another down-converted photon pair (A and B, and A and C, respectively, on figure 4.2). The second stage is the seeding: the signal photon in mode A produced by BBO1 is superpose and aligned with the optical path of the signal photon produced by BBO2. At this stage there are four photons in the device, two photons in mode A, and one photon each in modes B and C. The third stage is the interference: the four photons are mixed on 50:50 beam splitters (represented by the blue boxes) to produce the HOM effect. The final stage is the heralding on particular OAM superpositions: we use spatial-light modulators (SLMs) for the heralding of modes A and D, and to project the desired state between modes B and C. After projection the state is couple into single-mode fibers (yellow lines) connected to a detector. The elements L*number* are lenses with a focus length according to the number in front of the L. We use these lenses to focus the beam into the nonlinear crystals. We use the lenses also to map the crystal planes of BBO1 and BBO2 into SLMs, and to map the SLMs planes into the single-mode fibers.

L250 and L500, and L200 and L400, which represent lenses with focal length indicated by the number.

After the generation of hyperentangled states, by means of interference between the two nonlinear crystals and beam splitters, we have to measure them. SLMs with programmed phase masks, namely superpositions of OAM modes, are used to project hyperentangled states. Modes A and D are used for heralding the hyperentangled state. So, the hyperentangled state is measured on modes B and C.

6.2 Observation of hyperentangled states using interference and detection-basis control

Figure 6.2 shows three photographs of the down-conversion process on each crystal. In (a) we have the down-conversion process generated on BBO1. Picture (b) shows the down-conversion process generated on BBO2. In (c) we have the *seeded* down-conversion process on BBO2, where we superposed and aligned the idler beam generated by BBO1 (*the seed*) with the idler beam generated by BBO2. On the left side of Fig.6.2c we can see that the two idler beams are perfectly matched. If the connection between the two idler modes is broken, on the CCD camera we will see that *the seed* disappear remaining only the SPDC ring generated on BBO2. In the same sense, if we turn off the SPDC effect on the second crystal we only will see *the photon seed* on camera.

We state that the characteristic of our method is interference between two nonlinearities on two beam splitters (see Fig. 6.1) with a general heralding (detection) protocol on two of the four resulting modes. As we discussed in Ch. IV, the dimensionality and structure of the final entangled state $|\psi_f\rangle = {}_D\langle P|_A\langle P|\psi_3\rangle$ depends on the number of projector modes we choose and their amplitude values, see Eq. (4.18). In this expansion we can choose not

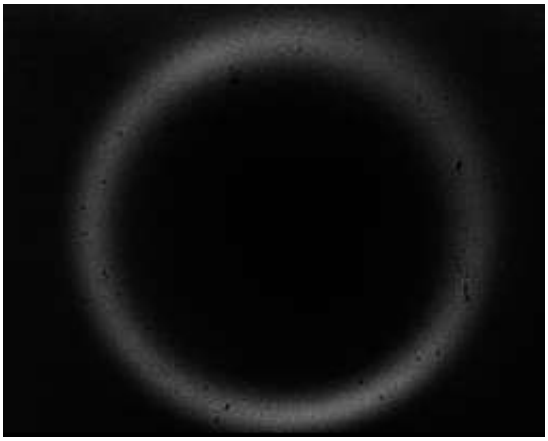

(a) Down-conversion process on BBO1

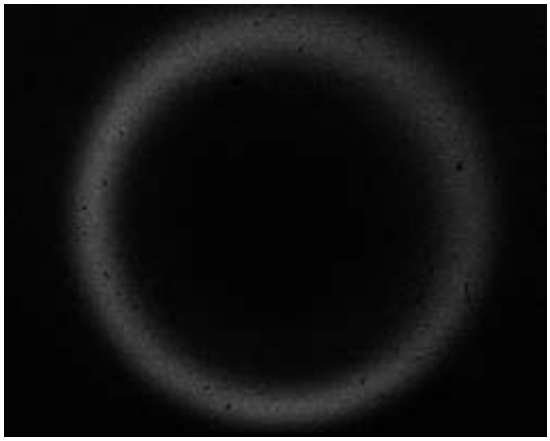

(b) Down-conversion process on BBO2

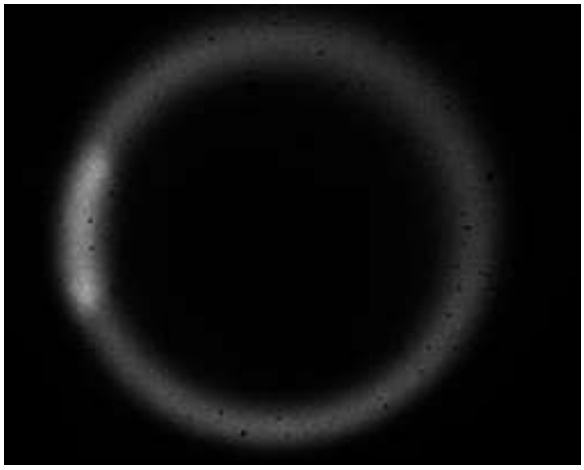

(c) Seeded down-conversion process on BBO2

Figure 6.2: Seeded spontaneous parametric down-conversion. (a) A photograph of the down-conversion process on the first crystal, BBO1. (b) A photograph of the down-conversion process on the second crystal, BBO2. (c) A photograph of the *seeded* down-conversion process on BBO2, where we superposed and aligned the idler photon generated by BBO1 (the seed) with the idler photon generated by BBO2. The seeded effect is shown on the left side of the picture.

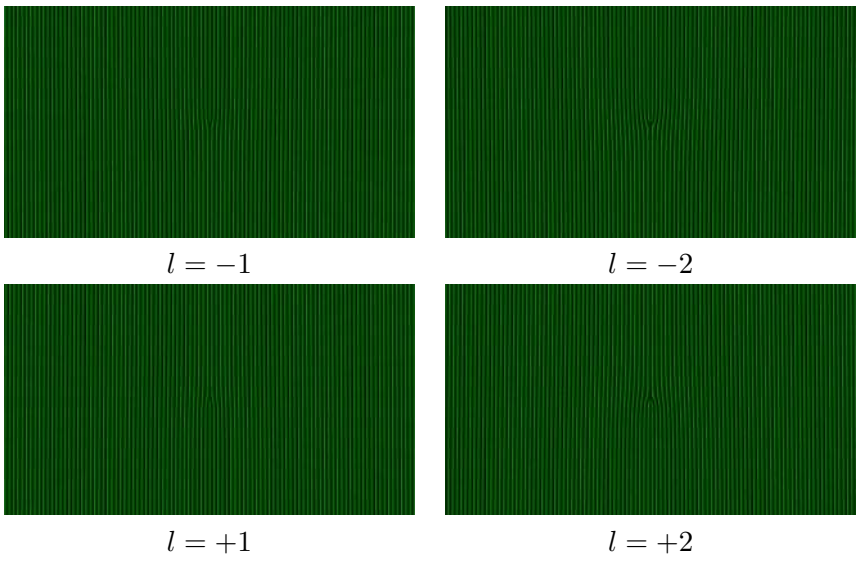

Figure 6.3: Phase masks for the measurement of orbital angular momentum of light.

only how many terms are in each superposition, but also the weights of all of those terms. We call this freedom *detection-basis control*. To measure the OAM of signal photons we first have to program it on SLMs with fork diffraction gratings. In the case of incident photons whose l-values are opposite to the holograms, the diffracted beam converts into a non-zero on-axis intensity that can be detected. Figure 6.3 shows examples of these fork diffraction gratings or phase masks with OAM values $l = \pm 1$ and ± 2.

In our experimental device, we use an SLM to program the desired state in which we want to project the state $|\psi_f\rangle$. This is done through a phase mask pattern with a specific phase on the hologram, or with a specific superposition of OAM modes. After projection, all the planes SLM-A, SLM-D, SLM-B and SLM-D are imaged to single-mode fibers (SMFs) using the group of coupling lenses L400, L100, L400 and an 8 mm lens (AL8). Each SMF is connected to a single-photon avalanche detector (SPAD, Excelitas) which is in turn connected to a coincidence detection system (IDQ 800). Since only the fundamental mode

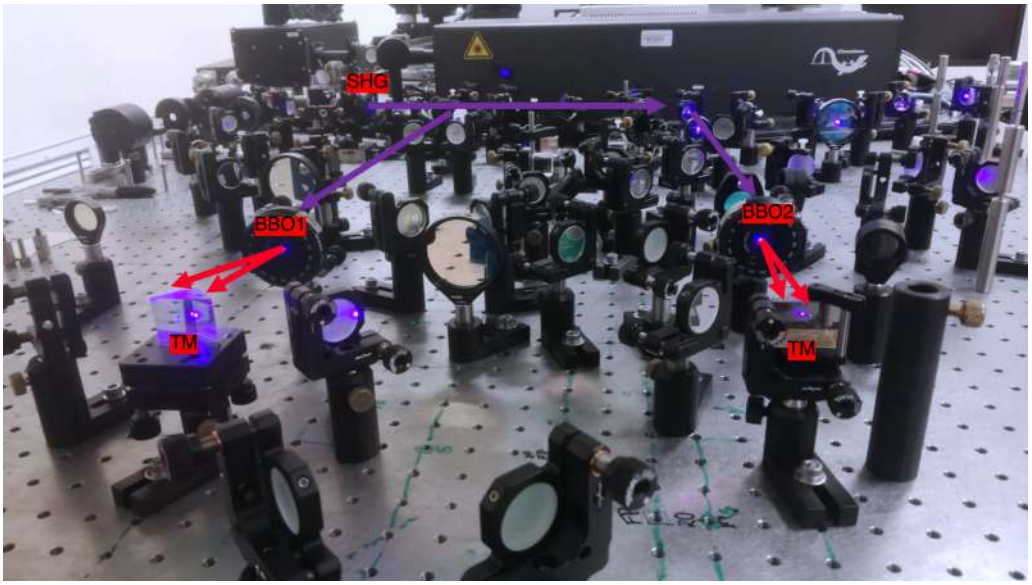

Figure 6.4: Photograph of the experimental setup. The purple arrows simulate the paths of the pump beam, and the red arrows simulate the paths of the photon pairs generated in each BBO crystal. SHG stand for second-harmonic generation, and TM for triangular mirror.

will couple to the fiber, a detector firing indicates a projection onto the programmed state. This system allows us to measure the generated hyperentangled state.

The measurements for the observation of hyperentangled states are underway. Figure 6.4 shows a picture of one part of the experimental setup. On the back of the picture we have the second-harmonic generation (SHG). The purple arrows illustrate the doubled frequency beam's path. BBO1 and BBO2 are the two nonlinear crystal that generate entangled photon pairs via SPDC. The red arrows illustrate the paths of the photon pairs generated in each BBO crystal.

CHAPTER VII

OUTLOOK

Our research focuses on spatial degrees of freedom for radial and orbital angular momentum (OAM) modes. We developed two methods for generating hyperentangled N00N states with OAM and radial modes. We have found that the optimization process in the preparation of the input beam is the current barrier to generating hyperentangled radial N00N states. In the context of generating high-dimensional hyperentangled OAM N00N states with detection-based control, the optimization process is also the current limitation to expanding beyond four dimensions.

Ch. III illustrates how the spatial spectrum of the down-converted state can be modulated by engineering the input beam. However, on the input beam, all the selections on the number of modes and their weights were made based on inspection. The next step is to optimize the weights of the input modes used, and take the data to higher dimensions using more terms to create other states. We also need to minimize the production and detection of the cross-correlated terms. In experimental settings, decreasing the detection-mode waist can reduce the detection of cross-correlated terms.

The detection-basis control method enable to project the states of both heralding modes on any superposition of OAM modes with any dimensionality. For example, we can select how many modes there are and how much weight they should carry. It is this characteristic that makes our protocol unique. For the cases we presented in Ch. V, however, all the selections on the number of modes and their weights were made by inspection. Therefore, the natural step is to expand to higher dimensions and optimize the weights on the projectors.

In order to optimize a model, there is a huge parameter space to search, unfortunately. Despite this opportunity, optimizing in high dimensions is challenging. Not only is it difficult to calculate minimum or maximum values with many parameters, but most distance concepts converge on similar values in higher dimensions. For example, due to the fact that projection of one vector onto another involves averaging values over each dimension, increasing the number of dimensions does not change the average value.

The state presented in Eq. (5.11), as we explained, is theoretically "perfect" and contains no unwanted terms. Such undesirable terms will almost certainly appear if we generalize over more dimensions. Some terms are simply noise, while others degrade entanglement, such as cross-terms between dimensions of the target state, which enable it to partially factorize. The same applies to our result from Ch. III, Eq. (3.19). For example, noise terms and cross-terms would not be distinguished by a direct state projection. Furthermore, whatever optimization process is used, it is essential to find a well-formed and useful metric.

It has been difficult to prove that states that are closely related to entangled states themselves share a similar amount of entanglement, but recent advances have made this possible. A state containing such entanglement is called "faithful". There has been research recently examining the faithfulness of entanglement [81, 82]. However, deciding the faithfulness of an entangled state is itself an optimization procedure. Therefore, a double optimization has to be done for any search to be successful.

Additionally, it may be interesting using other spatial modes, such as Hermite-Gauss or Bessel-Gauss, for the generation of hyperentangled N00N states. It may be also advantageous to study how pump beams can be controlled to achieve full control over the generated state, or to enhance the state making it more hyper using other degrees of freedom such as

frequency or polarization. The search for other entangled states of interest could also be aided by the application of machine learning techniques, which excel at pattern recognition and optimization.

CHAPTER VIII

SUMMARY AND CONCLUSIONS

We provided an overview of photonic quantum systems as a means for processing and communicating quantum information. We reviewed publications proposing a generation of hyperentangled states in both multiple degrees of freedom and one degree of freedom. We also analyzed experimental demonstrations of quantum protocols in low and high dimensions, with a focus on the spatial degree of freedom with radial and OAM modes. All these works motivated our research and set the theoretical framework.

The first approach was to investigate the Laguerre-Gauss radial modes for the generation of hyperentangled N00N states. Our findings illustrate how the spatial spectrum of the down-converted radial state can be modulated by engineering the input beam. We also found that the generation of radial states is noisy in nature. So cross-correlations are expected, and this limits the generation of clean, useful entangled states. Another limitation is the optimization process. There is a need for a better optimization process that controls the pump in terms of both the number of modes and their amplitudes (weights) based on down-converted target states.

Our method of generation of hyperentangled radial N00N states is not limited to radial modes. The method applied to orbital angular momentum modes, and any spatial-modes of light.

We presented a novel *detection-basis control* protocol for the generation of hyperentangled N00N states with orbital angular momentum and tunable dimensionality. In our device, we use two beam splitters and a coincidence detection protocol at their outputs to detect interference between the optical nonlinearities. A minimum of four dimensions of

hyperentanglement can be achieved with the down-converted OAM N00N state in this configuration.

Using specific superpositions of orbital angular momentum modes, we can also drastically alter the structure of output states and tune their dimensionality. OAM superpositions of two modes, for instance, can produce both two-dimensional entangled OAM N00N states as well as four-dimensional hyperentangled states by adjusting only their amplitude values. Consequently, the detection-basis control protocol allows the basis to be any spatial-basis in the Hilbert space, and creates new access to hyperentangled N00N states not only with orbital angular momentum, but also with other spatial-modes across a wide range of dimensions.

The experimental implementation of our protocol is underway.

BIBLIOGRAPHY

[1] M. Planck, "On the law of distribution of energy in the normal spectrum," *Annalen der physik*, vol. 4, no. 553, p. 1, 1901.

[2] A. Einstein, "Einstein's proposal of the photon conceptfia translation of the annalen der physik paper of 1905," *Ann. Physik*, vol. 17, p. 132, 1905.

[3] A. H. Compton, "A quantum theory of the scattering of x-rays by light elements," *Physical review*, vol. 21, no. 5, p. 483, 1923.

[4] L. De Broglie, "Waves and quanta," *Nature*, vol. 112, no. 2815, pp. 540–540, 1923.

[5] N. Gisin and R. Thew, "Quantum communication," *Nature photonics*, vol. 1, no. 3, pp. 165–171, 2007.

[6] T. E. Northup and R. Blatt, "Quantum information transfer using photons," *Nature Photonics*, vol. 8, no. 5, p. 356–363, 2014.

[7] A. Orieux and E. Diamanti, "Recent advances on integrated quantum communications," *Journal of Optics*, vol. 18, no. 8, p. 083002, 2016.

[8] E. Agrell, M. Karlsson, A. Chraplyvy, D. J. Richardson, P. M. Krummrich, P. Winzer, K. Roberts, J. K. Fischer, S. J. Savory, B. J. Eggleton, *et al.*, "Roadmap of optical communications," *Journal of Optics*, vol. 18, no. 6, p. 063002, 2016.

[9] J. S. Sidhu, S. K. Joshi, M. Gündoğan, T. Brougham, D. Lowndes, L. Mazzarella, M. Krutzik, S. Mohapatra, D. Dequal, G. Vallone, *et al.*, "Advances in space quantum communications," *IET Quantum Communication*, vol. 2, no. 4, pp. 182–217, 2021.

[10] F. Flamini, N. Spagnolo, and F. Sciarrino, "Photonic quantum information processing: a review," *Reports on Progress in Physics*, vol. 82, no. 1, p. 016001, 2018.

[11] X. Su, M. Wang, Z. Yan, X. Jia, C. Xie, and K. Peng, "Quantum network based on non-classical light," *Science China Information Sciences*, vol. 63, no. 8, pp. 1–12, 2020.

[12] A. Acín, I. Bloch, H. Buhrman, T. Calarco, C. Eichler, J. Eisert, D. Esteve, N. Gisin, S. J. Glaser, F. Jelezko, *et al.*, "The quantum technologies roadmap: a european community view," *New Journal of Physics*, vol. 20, no. 8, p. 080201, 2018.

[13] J. Roslund, R. M. De Araújo, S. Jiang, C. Fabre, and N. Treps, "Wavelength-multiplexed quantum networks with ultrafast frequency combs," *Nature Photonics*, vol. 8, no. 2, p. 109–112, 2014.

[14] J. L. O'brien, "Optical quantum computing," *Science*, vol. 318, no. 5856, pp. 1567–1570, 2007.

[15] M. Kjaergaard, M. E. Schwartz, J. Braumüller, P. Krantz, J. I.-J. Wang, S. Gustavsson, and W. D. Oliver, "Superconducting qubits: Current state of play," *Annual Review of Condensed Matter Physics*, vol. 11, pp. 369–395, 2020.

[16] A. Forbes and I. Nape, "Quantum mechanics with patterns of light: Progress in high dimensional and multidimensional entanglement with structured light," *AVS Quantum Science*, vol. 1, no. 1, p. 011701, 2019.

[17] H. Rubinsztein-Dunlop, A. Forbes, M. V. Berry, M. R. Dennis, D. L. Andrews, M. Mansuripur, C. Denz, C. Alpmann, P. Banzer, T. Bauer, *et al.*, "Roadmap on structured light," *Journal of Optics*, vol. 19, no. 1, p. 013001, 2016.

[18] M. Piccardo, V. Ginis, A. Forbes, S. Mahler, A. A. Friesem, N. Davidson, H. Ren, A. H. Dorrah, F. Capasso, F. T. Dullo, *et al.*, "Roadmap on multimode light shaping," *Journal of Optics*, vol. 24, no. 1, p. 013001, 2021.

[19] P. P. Rohde, J. F. Fitzsimons, and A. Gilchrist, "Information capacity of a single photon," *Physical Review A*, vol. 88, no. 2, p. 022310, 2013.

[20] H.-L. Huang, D. Wu, D. Fan, and X. Zhu, "Superconducting quantum computing: a review," *Science China Information Sciences*, vol. 63, no. 8, pp. 1–32, 2020.

[21] F. Arute, K. Arya, R. Babbush, D. Bacon, J. C. Bardin, R. Barends, R. Biswas, S. Boixo, F. G. Brandao, D. A. Buell, *et al.*, "Quantum supremacy using a programmable superconducting processor," *Nature*, vol. 574, no. 7779, pp. 505–510, 2019.

[22] R. P. Feynman, *Feynman and Computation: Exploring the Limits of Computers*. Westview Press, 1999.

[23] L. K. Grover, "A fast quantum mechanical algorithm for estimating the median," *arXiv preprint quant-ph/9607024*, 1996.

[24] P. W. Shor, "Polynomial-time algorithms for prime factorization and discrete logarithms on a quantum computer," *SIAM review*, vol. 41, no. 2, pp. 303–332, 1999.

[25] A. Babazadeh, M. Erhard, F. Wang, M. Malik, R. Nouroozi, M. Krenn, and A. Zeilinger, "High-dimensional single-photon quantum gates: Concepts and experiments," *Phys. Rev. Lett.*, vol. 119, p. 180510, Nov 2017.

[26] M. Kues, C. Reimer, P. Roztocki, L. R. Cortés, S. Sciara, B. Wetzel, Y. Zhang, A. Cino, S. T. Chu, B. E. Little, D. J. Moss, L. Caspani, J. Azaña, and R. Morandotti, "On-chip generation of high-dimensional entangled quantum states and their coherent control," *Nature*, vol. 546, no. 7660, pp. 622–626, 2017.

[27] M. Krenn, A. Hochrainer, M. Lahiri, and A. Zeilinger, "Entanglement by path identity," *Phys. Rev. Lett.*, vol. 118, p. 080401, Feb 2017.

[28] A. Mair, A. Vaziri, G. Weihs, and A. Zeilinger, "Entanglement of the orbital angular momentum states of photons," *Nature*, vol. 412, no. 6844, pp. 313–316, 2001.

[29] B. Jack, A. M. Yao, J. Leach, J. Romero, S. Franke-Arnold, D. G. Ireland, S. M. Barnett, and M. J. Padgett, "Entanglement of arbitrary superpositions of modes within two-dimensional orbital angular momentum state spaces," *Phys. Rev. A*, vol. 81, p. 043844, Apr 2010.

[30] M. Erhard, M. Malik, M. Krenn, and A. Zeilinger, "Experimental greenberger–horne–zeilinger entanglement beyond qubits," *Nature Photonics*, vol. 12, no. 12, pp. 759–764, 2018.

[31] E. V. Kovlakov, S. S. Straupe, and S. P. Kulik, "Quantum state engineering with twisted photons via adaptive shaping of the pump beam," *Phys. Rev. A*, vol. 98, p. 060301, Dec 2018.

[32] S. Liu, Z. Zhou, S. Liu, Y. Li, Y. Li, C. Yang, Z. Xu, Z. Liu, G. Guo, and B. Shi, "Coherent manipulation of a three-dimensional maximally entangled state," *Phys. Rev. A*, vol. 98, p. 062316, Dec 2018.

[33] S. Liu, Y. Zhang, C. Yang, S. Liu, Z. Ge, Y. Li, Y. Li, Z. Zhou, G. Guo, and B. Shi, "Increasing two-photon entangled dimensions by shaping input-beam profiles," *Phys. Rev. A*, vol. 101, p. 052324, May 2020.

[34] M. Hiekkamäki, F. Bouchard, and R. Fickler, "Photonic angular superresolution using twisted n00n states," *Phys. Rev. Lett.*, vol. 127, p. 263601, Dec 2021.

[35] F.-G. Deng, B.-C. Ren, and X.-H. Li, "Quantum hyperentanglement and its applications in quantum information processing," *Science bulletin*, vol. 62, no. 1, pp. 46–68, 2017.

[36] F. Graffitti, V. D'Ambrosio, M. Proietti, J. Ho, B. Piccirillo, C. De Lisio, L. Marrucci, and A. Fedrizzi, "Hyperentanglement in structured quantum light," *Physical Review Research*, vol. 2, no. 4, 2020.

[37] X. Gao, Y. Zhang, A. D'Errico, K. Heshami, and E. Karimi, "Tera-mode of spatiotemporal n00n states," 2021.

[38] J. Jackson, *Classical Electrodynamics*. Wiley, 1998.

[39] L. Allen, M. W. Beijersbergen, R. J. C. Spreeuw, and J. P. Woerdman, "Orbital angular momentum of light and the transformation of laguerre-gaussian laser modes," *Phys. Rev. A*, vol. 45, pp. 8185–8189, Jun 1992.

[40] M. A. Bandres and J. C. Gutiérrez-Vega, "Ince–gaussian beams," *Optics letters*, vol. 29, no. 2, pp. 144–146, 2004.

[41] S. N. Khonina, N. L. Kazanskiy, S. V. Karpeev, and M. A. Butt, "Bessel beam: Significance and applications—a progressive review," *Micromachines*, vol. 11, no. 11, p. 997, 2020.

[42] Z. Cheng, S. Zhao, X. Chu, B. Deng, and X. Zhang, "Research progress of the generation methods of airy beam," *Laser & Optoelectronics Progress*, vol. 52, no. 3, p. 030008, 2015.

[43] J. C. Gutiérrez-Vega, M. Iturbe-Castillo, and S. Chávez-Cerda, "Alternative formulation for invariant optical fields: Mathieu beams," *Optics letters*, vol. 25, no. 20, pp. 1493–1495, 2000.

[44] J. C. Guerra Vázquez, E. Narváez Castañeda, R. Ramírez Alarcón, I. Agha, Q. Zhan, and W. N. Plick, "Generation of four-dimensional hyperentangled noon states and beyond with photonic orbital angular momentum and detection-basis control," *Phys. Rev. A*, vol. 105, p. 032445, Mar 2022.

[45] S. Pachava, R. Dharmavarapu, A. Vijayakumar, S. Jayakumar, A. Manthalkar, A. Dixit, N. K. Viswanathan, B. Srinivasan, and S. Bhattacharya, "Generation and decomposition of scalar and vector modes carrying orbital angular momentum: a review," *Optical Engineering*, vol. 59, no. 4, p. 041205, 2019.

[46] K. Zhang, Y. Wang, Y. Yuan, and S. N. Burokur, "A review of orbital angular momentum vortex beams generation: From traditional methods to metasurfaces," *Applied Sciences*, vol. 10, p. 1015, Feb 2020.

[47] Y. Shen, X. Wang, Z. Xie, C. Min, X. Fu, Q. Liu, M. Gong, and X. Yuan, "Optical vortices 30 years on: Oam manipulation from topological charge to multiple singularities," *Light: Science & Applications*, vol. 8, no. 1, pp. 1–29, 2019.

[48] Z. Ibarra-Borja, C. Sevilla-Gutiérrez, R. Ramírez-Alarcón, Q. Zhan, H. Cruz-Ramírez, and A. B. U'Ren, "Direct observation of oam correlations from spatially entangled bi-photon states," *Opt. Express*, vol. 27, pp. 25228–25240, Sep 2019.

[49] G. Xie, Y. Ren, Y. Yan, H. Huang, N. Ahmed, L. Li, Z. Zhao, C. Bao, M. Tur, S. Ashrafi, *et al.*, "Experimental demonstration of a 200-gbit/s free-space optical link by multiplexing laguerre–gaussian beams with different radial indices," *Optics letters*, vol. 41, no. 15, pp. 3447–3450, 2016.

[50] I. Bialynicki-Birula and Z. Bialynicka-Birula, "Beams of electromagnetic radiation carrying angular momentum: The riemann–silberstein vector and the classical–quantum correspondence," *Optics communications*, vol. 264, no. 2, pp. 342–351, 2006.

[51] A. E. Willner, H. Huang, Y. Yan, Y. Ren, N. Ahmed, G. Xie, C. Bao, L. Li, Y. Cao, Z. Zhao, *et al.*, "Optical communications using orbital angular momentum beams," *Advances in optics and photonics*, vol. 7, no. 1, pp. 66–106, 2015.

[52] J. Wang, "Twisted optical communications using orbital angular momentum," *Science China Physics, Mechanics & Astronomy*, vol. 62, no. 3, pp. 1–21, 2019.

[53] M. J. Padgett, "Orbital angular momentum 25 years on," *Optics express*, vol. 25, no. 10, pp. 11265–11274, 2017.

[54] R. Chen, H. Zhou, M. Moretti, X. Wang, and J. Li, "Orbital angular momentum waves: generation, detection, and emerging applications," *IEEE Communications Surveys & Tutorials*, vol. 22, no. 2, pp. 840–868, 2019.

[55] J. Mejía-Salazar and O. N. Oliveira Jr, "Plasmonic biosensing: Focus review," *Chemical reviews*, vol. 118, no. 20, pp. 10617–10625, 2018.

[56] A. M. Yao, "Angular momentum decomposition of entangled photons with an arbitrary pump," *New Journal of Physics*, vol. 13, p. 053048, may 2011.

[57] V. Giovannetti, S. Lloyd, and L. Maccone, "Advances in quantum metrology," *Nature photonics*, vol. 5, no. 4, pp. 222–229, 2011.

[58] M. W. Mitchell, J. S. Lundeen, and A. M. Steinberg, "Super-resolving phase measurements with a multiphoton entangled state," *Nature*, vol. 429, no. 6988, pp. 161–164, 2004.

[59] C. K. Hong, Z. Y. Ou, and L. Mandel, "Measurement of subpicosecond time intervals between two photons by interference," *Phys. Rev. Lett.*, vol. 59, pp. 2044–2046, Nov 1987.

[60] Z. Y. Ou, "Fundamental quantum limit in precision phase measurement," *Phys. Rev. A*, vol. 55, pp. 2598–2609, Apr 1997.

[61] S. M. Barnett and R. Zambrini, "Resolution in rotation measurements," *Journal of Modern Optics*, vol. 53, no. 5-6, pp. 613–625, 2006.

[62] L. Allen, M. W. Beijersbergen, R. J. C. Spreeuw, and J. P. Woerdman, "Orbital angular momentum of light and the transformation of laguerre-gaussian laser modes," *Phys. Rev. A*, vol. 45, pp. 8185–8189, Jun 1992.

[63] D. Cozzolino, B. Da Lio, D. Bacco, and L. K. Oxenløwe, "High-dimensional quantum communication: Benefits, progress, and future challenges," *Advanced Quantum Technologies*, vol. 2, no. 12, p. 1900038, 2019.

[64] W. N. Plick, R. Lapkiewicz, S. Ramelow, and A. Zeilinger, "The forgotten quantum number: A short note on the radial modes of laguerre-gauss beams," 2013.

[65] A. D'Errico, F. Hufnagel, F. Miatto, M. Rezaee, and E. Karimi, "Full-mode characterization of correlated photon pairs generated in spontaneous downconversion," *Optics Letters*, vol. 46, no. 10, pp. 2388–2391, 2021.

[66] N. H. Valencia, V. Srivastav, S. Leedumrongwatthanakun, W. McCutcheon, and M. Malik, "Entangled ripples and twists of light: radial and azimuthal laguerre–gaussian mode entanglement," *Journal of optics*, vol. 23, no. 10, p. 104001, 2021.

[67] F. M. Miatto, A. M. Yao, and S. M. Barnett, "Full characterization of the quantum spiral bandwidth of entangled biphotons," *Phys. Rev. A*, vol. 83, p. 033816, Mar 2011.

[68] V. D. Salakhutdinov, E. R. Eliel, and W. Löffler, "Full-field quantum correlations of spatially entangled photons," *Phys. Rev. Lett.*, vol. 108, p. 173604, Apr 2012.

[69] E. Karimi, D. Giovannini, E. Bolduc, N. Bent, F. M. Miatto, M. J. Padgett, and R. W. Boyd, "Exploring the quantum nature of the radial degree of freedom of a photon via hong-ou-mandel interference," *Phys. Rev. A*, vol. 89, p. 013829, Jan 2014.

[70] E. Karimi, R. W. Boyd, P. de la Hoz, H. de Guise, J. Řeháček, Z. Hradil, A. Aiello, G. Leuchs, and L. L. Sánchez-Soto, "Radial quantum number of laguerre-gauss modes," *Phys. Rev. A*, vol. 89, p. 063813, Jun 2014.

[71] W. N. Plick and M. Krenn, "Physical meaning of the radial index of laguerre-gauss beams," *Phys. Rev. A*, vol. 92, p. 063841, Dec 2015.

[72] N. Sangouard, C. Simon, H. de Riedmatten, and N. Gisin, "Quantum repeaters based on atomic ensembles and linear optics," *Rev. Mod. Phys.*, vol. 83, pp. 33–80, Mar 2011.

[73] F. Bouchard, A. Sit, Y. Zhang, R. Fickler, F. M. Miatto, Y. Yao, F. Sciarrino, and E. Karimi, "Two-photon interference: the hong–ou–mandel effect," *Reports on Progress in Physics*, vol. 84, no. 1, p. 012402, 2020.

[74] X. Zou, L. J. Wang, and L. Mandel, "Induced coherence and indistinguishability in optical interference," *Physical review letters*, vol. 67, no. 3, p. 318, 1991.

[75] L. J. Wang, X. Y. Zou, and L. Mandel, "Induced coherence without induced emission," *Phys. Rev. A*, vol. 44, pp. 4614–4622, Oct 1991.

[76] M. Lahiri, R. Lapkiewicz, G. B. Lemos, and A. Zeilinger, "Theory of quantum imaging with undetected photons," *Physical Review A*, vol. 92, no. 1, p. 013832, 2015.

[77] Z. Y. Ou, L. J. Wang, X. Y. Zou, and L. Mandel, "Coherence in two-photon down-conversion induced by a laser," *Phys. Rev. A*, vol. 41, pp. 1597–1601, Feb 1990.

[78] C. Couteau, "Spontaneous parametric down-conversion," *Contemporary Physics*, vol. 59, no. 3, pp. 291–304, 2018.

[79] A. de Oliveira, N. Rubiano da Silva, R. Medeiros de Araújo, P. Souto Ribeiro, and S. Walborn, "Quantum optical description of phase conjugation of vector vortex beams in stimulated parametric down-conversion," *Phys. Rev. Applied*, vol. 14, p. 024048, Aug 2020.

[80] M. Krenn, M. Huber, R. Fickler, R. Lapkiewicz, S. Ramelow, and A. Zeilinger, "Generation and confirmation of a (100 x 100)-dimensional entangled quantum system," *Proceedings of the National Academy of Sciences*, vol. 111, no. 17, p. 6243–6247, 2014.

[81] O. Gühne, Y. Mao, and X.-D. Yu, "Geometry of faithful entanglement," *Phys. Rev. Lett.*, vol. 126, p. 140503, Apr 2021.

[82] X.-M. Hu, W.-B. Xing, Y. Guo, M. Weilenmann, E. A. Aguilar, X. Gao, B.-H. Liu, Y.-F. Huang, C.-F. Li, G.-C. Guo, *et al.*, "Optimized detection of high-dimensional entanglement," *Physical review letters*, vol. 127, no. 22, p. 220501, 2021.